PCCP

Detecting reactive islands in a system-bath model of isomerization

Journal:	*Physical Chemistry Chemical Physics*
Manuscript ID	CP-ART-03-2020-001362.R1
Article Type:	Paper
Date Submitted by the Author:	09-May-2020
Complete List of Authors:	Naik, Shibabrat; University of Bristol Faculty of Science, Mathematics Wiggins, Stephen; University of Bristol Faculty of Science, Mathematics

PCCP

ROYAL SOCIETY OF CHEMISTRY

ARTICLE TYPE

Cite this: DOI: 10.1039/xxxxxxxxxx

Detecting reactive islands in a system-bath model of isomerization†

Shibabrat Naik,*[a] Stephen Wiggins,[b‡]

Received Date
Accepted Date

DOI: 10.1039/xxxxxxxxxx

www.rsc.org/journalname

In this article, we study the conformational isomerization in a solvent using a system-bath model where the phase space structures relevant for the reaction dynamics are revealed. These phase space structures are an integral part of understanding the reaction mechanism, that is the pathways that reactive trajectories undertake, in the presence of a solvent. Our approach involves detecting the analogs of the reactive islands first discussed in the works by Davis, Marston, De Leon, Berne and coauthors [1–4] in the system-bath model using Lagrangian descriptors. We first present the structure of the reactive islands for the two degrees of freedom system modelling isomerization in the absence of the bath using direct computation of cylindrical (*tube*) manifolds and verify the Lagrangian descriptor method for detecting the reactive islands. The hierarchy of the reactive islands as indicated in the recent work by Patra and Keshavamurthy [5] is shown to be related to the temporal features in committor probabilities. Next, we investigate the influence of the solvent on the reactive islands that we previously revealed for the two degrees of freedom system and discuss the use of the Lagrangian descriptor in the high-dimensional phase space of the system-bath model.

1 Introduction

Isomerization is an important reaction in atmospheric, medical, and industrial chemistry * [6–9]. On one hand, the influence of various solvents on the rate constant of conformational isomerization has been pursued for specific molecules [10–14] using statistical mechanics. On the other hand, dynamical systems theory has been used to develop a systematic approach for identifying trajectories that go from reactants to products and reside inside phase space structures called *reactive islands* in two degrees of freedom Hamiltonian models [1–4]. In this article, we extend the reactive islands approach to $N > 2$ degrees of freedom model for the isomerization reaction in a bath.

Following the derivation of the Langevin equations and its generalized system dynamics in a heat bath [15], Kramers [16] derived the expression for the escape rate of a Brownian particle trapped in a potential well for small and large values of the viscosity. He also showed that only for a specific potential barrier the escape rate for all values of viscosity is equal to the one given by the transition state theory. However, the solution for all values of viscosity was obtained in 1980s by Mel'nikov, Meshkov [17] and Grote, Hynes, Pollak, Grabert, Hänggi [18,19] and showed the turnover of reaction rates with the increasing viscosity of the solvent. Furthermore, Pollak's derivation [20] connected the Kramers theory and the transition state theory for condensed phase reactions which has been useful for calculations of rate expressions [21]. These developments established the Langevin equation of motion for a particle trapped in a potential well with a barrier height $\mathscr{V}^{\ddagger}$ as a model for studying a reaction in the condensed phase. In this set-up, the reaction (or the system) is defined by the crossing of the barrier and the influence of the medium (or the bath) is studied by coupling the bath coordinates to the system coordinates. This framework has received much attention in the literature where the system dynamics can be obtained explicitly using a one-dimensional potential well and the bath is modelled using a large number of harmonic oscillators with mass, frequency, and viscosity parameters [22–25]. In this set-up, the bath coordinates are coupled with the system coordinates via the viscosity (or the friction) parameter in the form of a bilinear term in the potential energy. This gives rise to the Hamiltonian which is written as a sum of kinetic energy and potential energy in the system and bath coordinates.

However, the dynamics of a two or more degrees of freedom system coupled with bath modes has not received a global analysis from a dynamical systems perspective of reactions. In this direction, the first step would be to consider a two degrees of freedom Hamiltonian system with well-understood quantities such as

[a] *School of Mathematics, University of Bristol*
Fry Building, Woodland Road, Bristol BS8 1UG, United Kingdom. Tel: XX XXXX XXXX; E-mail: s.naik@bristol.ac.uk
[b] *s.wiggins@bristol.ac.uk.*

† Electronic Supplementary Information (ESI) available: Derivation of equations of motion and the computational approach to obtain the cylindrical manifolds.

* https://www.sciencedirect.com/topics/engineering/isomerization

the *reaction coordinate*, and to which the harmonic bath modes can be coupled to represent the reaction in a condensed phase. In this work, we will adopt the two degrees of freedom isomerization model of De Leon and Berne who studied the chemical reaction dynamics extensively using a dynamical systems perspective[4,26–30]. This Hamiltonian model of isomerization describes the conformational change by the motion of an internal angle where the isomers are represented by the wells in a double potential well separated by a barrier. The two degrees of freedom in the model correspond to the bond that undergoes rotation (structural change of a molecule) for total energies between the isomerization and dissociation energy and to the bond that splits above dissociation energy. Typically, the isomerization energy is lower than the dissociation energy of the molecule, and the activation energy for the isomerization is imparted by molecular collisions or photoexcitation.

Traditionally, the construction of a dividing surface (DS) was focused on critical points of the potential energy surface (PES), that is, in the configuration space describing the molecular system[31]. Critical points on the PES do have significance in phase space since they are the equilibrium points for zero momentum. But they continue to have influence for nonzero momentum for a range of energies above the energy of the equilibrium point. The construction of a DS separating the phase space into two parts, that is reactants and products, has been a focus from the dynamical systems point of view in recent years[32–34]. In phase space, the role of the *saddle equilibrium point* is played by an *invariant manifold* of saddle type stability called the normally hyperbolic invariant manifold (NHIM)[35,36]. In order to fully appreciate the NHIM and its role in reaction rate theory, it is useful to begin with a precursor concept — the *periodic orbit dividing surface* or PODS. For systems with two DOF described by a natural Hamiltonian, kinetic plus potential energy, the problem of constructing the DS in phase space was solved during the 1970s by McLafferty, Pechukas and Pollak[37–40]. They demonstrated that the DS at a specific energy is related to an invariant phase space structure, an unstable periodic orbit (UPO) which defines (it is the boundary of) the bottleneck in phase space through which the reaction occurs. The DS which intersects trajectories evolving from reactants to products can then be shown to have the geometry of a hemisphere in phase space whose boundary is the UPO. The same construction can be carried out for a DS intersecting trajectories crossing from products to reactants and these two hemispheres form a sphere for which the UPO is the equator. Generalisation of this construction of DS to high dimensional systems has been a central question in reaction dynamics and has only received a satisfactory answer in recent years[32–34]. The key difficulty being the high dimensional analogue of the UPO used in the two DOF system for the construction of the DS and which is resolved by considering the NHIM, which has the appropriate dimensionality for anchoring the dividing surface in high dimensional phase space[35]. Normal hyperbolicity of these invariant manifolds means that their stability, in a precise sense, is of saddle type in the transverse direction, which implies that they possess stable and unstable invariant manifolds that are impenetrable barriers and mediate reactive trajectories in phase space. These invariant manifolds of the NHIM are structurally stable, that is, stable under perturbation[36]. For two DOF systems, the NHIM is an unstable PO, and for an $N > 2$ DOF system at a fixed energy, the NHIM has the topology of a $(2N-3)$-dimensional sphere and is the equator of a $(2N-2)$-dimensional sphere which is the DS. This DS can then be used to divide the $(2N-1)$-dimensional energy surface into two parts, reactants and products[41–45]. An elementary description of the role of the NHIM in reaction dynamics is given in[46] along with description of their geometry using quadratic normal form Hamiltonians. Fundamental theorems assure the existence of the phase space structures — NHIM and its invariant manifolds —for a range of energies above that of the saddle[36]. However, the precise extent of this range, as well as the nature and consequences of any bifurcations of the phase space structures that might occur as energy is increased, is not known and is a topic of continuing research[47–52].

Thus, calculation of reaction rate (or flux) based on the geometry of phase space structures requires identifying trajectories that start in the *reactant* well, cross the dividing surface constructed from the NHIM, and reach the *product* well. This dividing surface has been shown to be the appropriate (locally no-recrossing) surface that reactive trajectories must cross since the calculated reaction rates do not need correction due to recrossings[34]. This construction is in contrast to the "standard" transition state theory (TST) for constructing the dividing surface which is only exact in gas phase unimolecular reactions and when ergodicity of trajectories in the phase space holds[19]. As is now established, the no recrossing (locally) property of a dividing surface is a contribution of the phase space perspective of chemical reactions[33]. While the standard TST relies on a recrossing free surface for calculating reaction flux, a dividing surface constructed in the configuration space violates this condition in the case of a solvent[19,53], and thus the TST based reaction rate is not exact. This violation of the recrossing property when the DS is constructed in the configuration space of a reaction in a high viscosity solvent also follows from the Kramers' diffusion model, Langevin equation, of chemical reactions[19]. Thus, finding the reactive trajectories, and the changes in the DS and NHIM is a worthwhile step towards understanding the phase space structures relevant for a reaction in a solvent.

For a general introduction to the theory and terminologies used in this study, we refer the reader to the excellent reviews[21,54] and the open source book on chemical reactions and dynamical systems[55]. The phase space geometry of unimolecular reactions dynamics has been developed using a two degrees of freedom Hamiltonian where the coordinates represent intermolecular bonds[3,4,26–30]. As a natural next step in studying unimolecular reaction dynamics in solvents, we adopt a model where the reaction coordinates (modeled as a system Hamiltonian) are coupled with a set of harmonic bath modes (modeled as a bath Hamiltonian)[56–59]. This is with the intention of parametrizing the effects of a solvent on the reaction dynamics. This formulation of coupling harmonic bath modes with system dynamics also serves as a preliminary step in assessing the capabilities of a trajectory diagnostic called Lagrangian descriptors (LDs)[60] in *realistic* (high dimensional) chemical systems. Lagrangian descriptors have been shown to detect phase space structures that mediate reactive tra-

jectories in dissipative, time-dependent models of chemical reactions[61,62], for transition path sampling in two degrees of freedom models of chemical reactions[5,63], and for revealing roaming pathways in molecular dissociation[64,65].

To find all the reactive trajectories at a given energy so they can be used in reaction rate calculations, one starts with some seed initial conditions that lead to reaction, and then produces more initial conditions (reactive) by varying the position and momenta. Hence this approach is phrased as harvesting reactive trajectories[63] in transition path sampling methods[66]. In high dimensional molecular phase space, this is a non-trivial computation due to the large size of the energetically accessible phase space volume. Since it has been shown that the reactive islands and their hierarchical structure can be used to search for reactive trajectories using the shooting method[5] in two degrees of freedom model, it is useful to consider how the same approach performs in a high dimensional system-bath model. The system-bath model will also serve as a test bed for illustrating the use of LDs in detecting the reactive islands in the presence of a solvent.

This article is outlined as follows. First, we briefly describe the De Leon-Berne Hamiltonian in § 2.1 and the corresponding system-bath Hamiltonian in § 2.2. This is followed by a description of the methods — Lagrangian descriptor and committor probability — in § 2.3. In § 3.1, we first present results on the system dynamics modelled by the De Leon-Berne Hamiltonian. Then, in § 3.1.1, we present a method for directly constructing the reactive islands and in § 3.1.2 we verify that the singular features in LD contour maps detect the reactive islands' boundaries by comparing it with the direct construction. Then, we make the connection with the temporal features in committor probabilities and the hierarchy of reactive islands in the system dynamics. Next, in § 3.2, we apply the approach of the LD based detection to find the hierarchy of reactive islands in the system-bath model along with verifying the results using the committor probability calculations. Then, we conclude with a summary and outlook in § 4.

2 Models and Methods

2.1 System dynamics: Two degrees of freedom isomerization

We consider the two degrees of freedom Hamiltonian for a unimolecular conformational isomerization introduced by De Leon, Berne and co-authors[4,26–28,30,67]. This system model describes the structural change of a molecule that goes from the isomer A to B and described by the reaction

$$A \underset{\text{backward}}{\overset{\text{forward}}{\rightleftarrows}} B. \tag{1}$$

The two degrees of freedom De Leon-Berne Hamiltonian is given by

$$\begin{aligned}\mathscr{H}(x,y,p_x,p_y) =& T(p_x,p_y)+V_{\mathrm{DB}}(x,y)\\ =& \frac{p_x^2}{2m_x}+\frac{p_y^2}{2m_y}+V_{\mathrm{DB}}(x,y)\end{aligned} \tag{2}$$

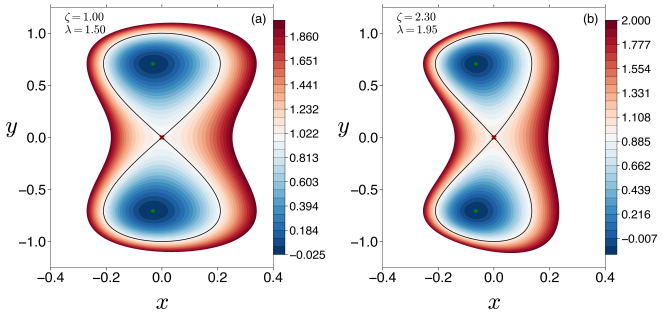

Fig. 1 Contour plot of the potential energy in the De Leon-Berne model of unimolecular isomerization[26,27] for the coupling and Morse range values shown and $\varepsilon_s = 1.0, D_x = 10.0, y_w = \pm 1/\sqrt{2}$ are used in both the plots. The location of the saddle equilibrium point (denoted by the red cross) is independent of the parameters and is always located at the origin, while the y-coordinate of the center equilibrium point is at y_w, the x-coordinate is dependent on the parameters.

where the potential energy function $V_{\mathrm{DB}}(x,y)$ is

$$\begin{aligned}V_{\mathrm{DB}}(x,y) =& D_x\left[1-\exp(-\lambda x)\right]^2\\ &+\frac{\mathscr{V}^{\ddagger}}{y_w^4}y^2(y^2-2y_w^2)\exp(-\zeta\lambda x)+\varepsilon_s\end{aligned} \tag{3}$$

and a description of the parameters is given in the Appendix A. In this study, we fix $\mathscr{V}^{\ddagger} = 1.0, y_w = \pm 1/\sqrt{2}, \varepsilon_s = 1.0, D_x = 10.0$, and vary the Morse range parameter, λ, and the coupling parameter, ζ, while using the same value for the mass of the system coordinates: $m_x = m_y = 8.0$ as adopted in the works of De Leon, Berne and co-authors[4,26–28,30,67]. We note that, in general, an isomerization reaction the representative system coordinates will have different mass parameter values, we have adopted the same value for both the coordinates to compare with known results on the De Leon-Berne Hamiltonian. The contour plots of the potential energy (3) for the chosen values of the range and coupling parameters are shown in Fig. 1. The Hamilton's equations are:

$$\begin{aligned}\dot{x} &= \frac{\partial\mathscr{H}}{\partial p_x} = \frac{p_x}{m_x}\\ \dot{y} &= \frac{\partial\mathscr{H}}{\partial p_y} = \frac{p_y}{m_y}\\ \dot{p_x} &= -\frac{\partial\mathscr{H}}{\partial x} = 2D_x\lambda\exp(-\lambda x)(\exp(-\lambda x)-1)\\ &\quad+\frac{\mathscr{V}^{\ddagger}}{y_w^4}\zeta\lambda y^2(y^2-2y_w^2)\exp(-\zeta\lambda x)\\ \dot{p_y} &= -\frac{\partial\mathscr{H}}{\partial y} = -4\frac{\mathscr{V}^{\ddagger}}{y_w^4}y(y^2-y_w^2)\exp(-\zeta\lambda x).\end{aligned} \tag{4}$$

Equilibrium points and total energy. The equilibrium points of the Hamiltonian vector field (4) are located at $\bar{q}_s = (0,0,0,0)$ and at $\bar{q}_c = (x_{eq}, \pm y_w, 0, 0)$ where the x-coordinate, x_{eq}, depends on the parameters chosen and is obtained using numerical root solver. The product is specified in the computations by the $y-$coordinate, $y_w = -1/\sqrt{2}$, and this condition that the product is specified by

the value of the bond that undergoes rotational change.

The total energy is denoted by $\mathscr{H}(x,y,p_x,p_y) = E = E_{\text{saddle}} + \Delta E$ where ΔE is the excess energy above the isomerization barrier energy. The total energy of the equilibrium point $\overline{q}_s$ is $\mathscr{H}(\overline{q}_s) = \varepsilon_s$ for all parameter values, and will be referred to as the *critical energy* or the isomerization barrier energy. The total energy of the equilibrium point $\overline{q}_c$ is given by

$$\mathscr{H}(\overline{q}_c) = D_x(1-\exp(-\lambda x_{eq}))^2 - \mathscr{V}^{\ddagger}\exp(-\zeta\lambda x_{eq}) + \varepsilon_s \qquad (5)$$

When the two degrees of freedom are uncoupled, that is $\zeta = 0$, the equilibrium point $\overline{q}_c$ is at $(0,\pm y_w,0,0)$, and has total energy $\varepsilon_s - \mathscr{V}^{\ddagger}$. Furthermore, since the total energy at these points (5) is independent of y_w, the total energy of the isomer state A and B is always same which makes this a symmetric double well potential. However, as we will show this configuration space symmetry does not imply symmetry in the backward and forward reaction defined by going from the top to the bottom well (Fig. 1).

2.2 System-bath dynamics: Two degree of freedom isomerization in a solvent

In this section we describe the system-bath model for a system with two degree of freedom (DOF). This type of system-bath model have been used to develop dynamical methods for a system coupled to an environment[68–70]. These theoretical of chemical reactions have been studied in the context for energy and charge transfer reactions[71], isomerization via conical intersection where the two active DOF are coupled to the environment[72]. We consider the two degree of freedom Hamiltonian (2) coupled with harmonic oscillators for a system-bath model of the form[56–58]:

$$\mathscr{H}(x,y,x_j,y_j,p_x,p_y,p_{x_j},p_{y_j}) =$$
$$\underbrace{\frac{p_x^2}{2m_x}+\frac{p_y^2}{2m_y}+V_{DB}(x,y)}_{\text{System Hamiltonian}} + \underbrace{\sum_{j=1}^{N_B}\frac{1}{2}\left[\frac{p_{x_j}^2}{m_j}+\left(\omega_j x_j - \frac{c_{x,j}x}{\omega_j}\right)^2\right]}_{\text{Coupling of the bath to } x}$$
$$+ \underbrace{\sum_{j=1}^{N_B}\frac{1}{2}\left[\frac{p_{y_j}^2}{m_j}+\left(\omega_j y_j - \frac{c_{y,j}y}{\omega_j}\right)^2\right]}_{\text{Coupling of the bath to } y}$$

where x and y denote the configuration space coordinates of the system, p_x and p_y are the associated conjugate momenta, p_{x_j}, x_j denote the j^{th} bath phase space coordinates associated with the system configuration space variable x, and p_{y_j}, y_j denote the j^{th} bath phase space coordinates associated with the system configuration space variable y. We assume that the frequencies, ω_j, are the same for each bath, and the coupling constants for each configuration space variable to the bath are given by $c_{x,j}$ and $c_{y,j}$. In the supplemental material, we explicitly carry out the discretization that gives us the coupling constants $c_{x,j}$ and $c_{y,j}$ and the frequencies ω_j. These quantities are given by

$$\omega_j = -\omega_c \log\left(\frac{j-\frac{1}{2}}{N_B}\right), \quad j = 1,\ldots,N_B \qquad (6)$$

and

$$c_{x,j} = \sqrt{\frac{2\eta_x\omega_c}{\pi N_B}}\,\omega_j, \;\; c_{y,j} = \sqrt{\frac{2\eta_y\omega_c}{\pi N_B}}\,\omega_j, \quad j = 1,\ldots,N_B. \qquad (7)$$

We note here that the bath modes are coupled to each other indirectly through the system dynamics and their coupling to the system coordinates depends on both the friction and frequency parameters.

Using Eqn. (3) and Eqn. (6), the Hamilton's equations for the system-bath model are:

$$\begin{aligned}
\dot{x} &= \frac{\partial\mathscr{H}}{\partial p_x} = \frac{p_x}{m_x},\\
\dot{y} &= \frac{\partial\mathscr{H}}{\partial p_y} = \frac{p_y}{m_y},\\
\dot{x}_j &= \frac{\partial\mathscr{H}}{\partial p_{x_j}} = \frac{p_{x_j}}{m_j}, \qquad j = 1,\ldots,N_B\\
\dot{y}_j &= \frac{\partial\mathscr{H}}{\partial p_{y_j}} = \frac{p_{y_j}}{m_j}, \qquad j = 1,\ldots,N_B,\\
\dot{p}_x &= -\frac{\partial\mathscr{H}}{\partial x} = 2D_x\lambda\exp(-\lambda x)(\exp(-\lambda x)-1)\\
&\quad + \frac{\mathscr{V}^{\ddagger}}{y_w^4}\zeta\lambda y^2(y^2-2y_w^2)\exp(-\zeta\lambda x)\\
&\quad + \sum_{j=1}^{N_B}\frac{c_{x,j}}{\omega_j}\left(\omega_j x_j - \frac{c_{x,j}x}{\omega_j}\right),\\
\dot{p}_y &= -\frac{\partial\mathscr{H}}{\partial y} = -4\frac{\mathscr{V}^{\ddagger}}{y_w^4}y(y^2-y_w^2)\exp(-\zeta\lambda x)\\
&\quad + \sum_{j=1}^{N_B}\frac{c_{y,j}}{\omega_j}\left(\omega_j y_j - \frac{c_{y,j}y}{\omega_j}\right),\\
\dot{p}_{x_j} &= -\frac{\partial\mathscr{H}}{\partial x_j} = -\omega_j\left(\omega_j x_j - \frac{c_{x,j}x}{\omega_j}\right), \quad j = 1,\ldots,N_B\\
\dot{p}_{y_j} &= -\frac{\partial\mathscr{H}}{\partial y_j} = -\omega_j\left(\omega_j y_j - \frac{c_{y,j}y}{\omega_j}\right), \quad j = 1,\ldots,N_B,
\end{aligned} \qquad (8)$$

where the bath frequencies ω_j and coupling coefficients $c_{x,j}, c_{y,j}$ are given by Eqn. (6) and Eqn. (7), respectively. The total energy will be denoted by $\mathscr{H}(x,y,x_j,y_j,p_x,p_y,p_{x_j},p_{y_j}) = E = E_{\text{saddle}} + \Delta E$ where $j = 1,2,\ldots,N_B$ and ΔE is the excess energy with respect to the isomerization barrier energy. In this article, we are adopting $\mathbf{x}$ to denote the x-coordinates of the bath modes $x_1,x_2,\ldots,x_{N_B}$; $\mathbf{p_x}$ to denote the x-momentum of the bath modes $p_{x_1},p_{x_2},\ldots,p_{x_{N_B}}$, and so forth.

In this form of coupling each system degree of freedom (N_S) is coupled with all its bath modes (N_B), the total number of degrees of freedom are $N_S + N_S N_B$, and thus the dimension of phase space is $2N_S(N_B+1)$. This gives us a high dimensional Hamiltonian model where we can increase the number of degrees of freedom by increasing the number of bath modes along with incorporating the effects of a solvent in a systematic way by chang-

ing the mass, frequency, and friction parameters. In this study, we will focus on a small value of the mass parameter and use 64 bath modes which amounts to a weak strength solvent or a small perturbation to the system dynamics. Although, the number of bath modes considered here are not large enough to capture the effect of a solvent in the Langevin sense, this formulation can be extended as long as enough computational time is reserved to obtain trajectories and the associated diagnostic method. However, the high dimensionality of the system-bath model will be a setting to assess how the method of Lagrangian descriptors performs in more realistic chemical systems. This also gives a natural way to model the unimolecular conformational isomerization in a solvent and allows us to vary the friction of the environment from low-density gases to high-density liquids[25].

Equilibrium points and total energy. The equilibrium points of the system-bath model (8) are located at $\overline{q}_s = (0,0,\mathbf{0},\mathbf{0},0,0,\mathbf{0},\mathbf{0})$ and at

$$\overline{q}_c = (x_{eq}, \pm y_w, (c_{x,j}/\omega_j^2)x_{eq}, (c_{y,j}/\omega_j^2)y_w, 0,0,\mathbf{0},\mathbf{0}), j = 1,\ldots,N_B. \tag{9}$$

where $\mathbf{0}$ is a vector of zeros of length N_B, x_{eq} is the x-coordinate of the equilibrium point in the system model and needs to be obtained using numerical methods for solving roots of nonlinear equations.

The linear stability analysis of the equilibrium point at the origin is shown in the Appendix E and we checked that the equilibrium point at the origin is an index-1 saddle with eigenvalues $\pm\lambda, \pm i\omega_1, \pm i\omega_2, \ldots, \pm i\omega_{N_S N_B+(N_S-1)}$. Thus, adding the bath modes in the form of Eqn. (6) has not changed the stability of the equilibrium points in the system Hamiltonian. We note that the structure of the Jacobian of the Hamilton's equations (8) (or the Hessian of the potential energy) is similar to the collected effective modes approach used in charge transfer reactions[68–71,73]. Next, the total energy of the index-1 saddle equilibrium point at $\overline{q}_s$ is $\mathscr{H}(0,0,\mathbf{0},\mathbf{0},0,0,\mathbf{0},\mathbf{0}) = \varepsilon_s$ which is also same. However, the coordinates of the well depend on the bath parameters and we check their stability in the Appendix E. To investigate the reaction dynamics, we will use an isoenergetic two-dimensional surface (to compute Lagrangian descriptors) at the well location in the system Hamiltonian even when the system-bath model is used so we can compare the phase space structures directly.

2.3 Methods

a. Lagrangian descriptor (LD) to detect the invariant manifolds As described in the Appendix C and presented in the literature[74–76], we know the singular features in the LD contour maps identify points on the invariant manifolds such as the normally hyperbolic invariant manifold and its associated stable and unstable manifolds. Since the reactive islands are formed by the stable and unstable manifolds, the boundary of the reactive islands can be identified in the LD contour map. We note here that both the fixed (49) and variable (53) integration time LD detect the reactive island structure except with some differences. Briefly, the former approach shows singular features in the contour map that are local *minima*, while the latter approach shows singular features in the contour map that are local *maxima*. Since the variable integration approach stops trajectories when they reach or leave a *preselected* region, the computations are faster than the fixed integration approach.

b. Committor probability to verify the reactive island structure Committor probability of a set of initial conditions, $(\mathbf{Q},\mathbf{P})$ where $\mathbf{Q},\mathbf{P} \in \mathbb{R}^N$ for N degrees of freedom system, is the fraction of trajectories that are committed to a stable state (this corresponds to the center equilibrium point or minima of the potential energy surface) B at a time t before reaching another stable state A. This is denoted by $P_B(t,(\mathbf{Q},\mathbf{P}))$ to check the committor probability of B when the initial conditions are fixed in A. This is calculated by launching N initial conditions with fixed position coordinates $\mathbf{Q}$ (this fixes the configuration of a molecule) and choosing momenta to satisfy the fixed energy constraint. Then, fraction of the initial conditions and the time until which the initial conditions remain committed to B is recorded, thus the committor probability for a stable state B becomes

$$P_B(t,(\mathbf{Q},\mathbf{P})) \approx \frac{1}{N}\sum_{i=1}^{N} \delta_B(\Phi_t(\mathbf{Q},\mathbf{P})), \tag{10}$$

where $\delta_B(\mathbf{Q},\mathbf{P})$ is the characteristic function of stable state B and $\Phi_t(\mathbf{Q},\mathbf{P})$ denotes the evolution of the initial conditions for time t under the Hamiltonian vector field, either (2) or (8). In this study, the system dynamics being described by the De Leon-Berne Hamiltonian, we choose the top well's $y-$coordinate as the state A ($y_w = 1/\sqrt{2}$) and bottom well's $y-$coordinate to be the state B ($y_w = -1/\sqrt{2}$).

Thus, committor probability is an approach to check which initial conditions become reactive trajectories and how long they spend in the reactant or product well. This amounts to checking the effectiveness of a method in sampling reaction (transition) paths in the phase space for a fixed energy. Therefore, it has been used for detecting reactive trajectories which are rare events when the energy of the barrier is higher than the energy imparted to the solute by the collisions with the solvent molecule. Since finding these reactive trajectories constitutes detecting rare events in the high dimensional phase space[5,77] of the system-bath model (8), we can test the effectiveness of the reactive islands in producing reactive trajectories in the system-bath model.

3 Results and discussion

3.1 System dynamics

The regular and chaotic dynamics of the Hamiltonian (2) and its implications for reaction rates has been studied in detail by Davis, Marston, De Leon, Berne and coauthors in the 1980s[1–4,26,27]. They have illustrated by varying the coupling parameter, ζ, and Morse range parameter, λ, that the simple model of isomerization can exhibit a wide variety of dynamically different trajectories. These manifest qualitatively as transition to chaos, coexistence of regular and chaotic regions, and quantitatively in the temporal decay of reaction rates. Further discussions of the reactions dynamics by varying the above parameters can be found in the open source book[55].

In this study, we will focus on the two sets of the coupling and range parameters: $\zeta = 1.00, \lambda = 1.50$ and $\zeta = 2.30, \lambda = 1.95$ to discover the reactive islands as shown in the literature and understand the influence of a solvent on the isomerization by studying the reactive islands. This approach of studying the influence of an environment on known reactions can be considered as an assessment of the LD contour map method for realistic reactions. Here we will demonstrate the use of Lagrangian descriptors for finding reactive islands in the system dynamics and verify the results using a direct construction of the global stable and unstable manifolds associated with the index-1 saddle equilibrium point. Our results of the reactive islands in the system dynamics applies to all the other parameter values in the literature and for an arbitrary total energy between the isomerization ($V^{\ddagger}$) and dissociation energy (D_x).

Poincaré surface of section — Let $\mathscr{M}(E)$ be the energy surface given by setting the Hamiltonian (2) or the total energy to a constant, that is

$$\mathscr{M}(E) = \left\{ (x, y, p_x, p_y) \in \mathbb{R}^4 \mid \mathscr{H}(x, y, p_x, p_y) = E \right\} \tag{11}$$

where E is the constant and the surface $\mathscr{M}(E)$ is three-dimensional and embedded in the four-dimensional phase space, $\mathbb{R}^4$, and thus referred to as codimension-1. Now, if we take a cross-section of this three-dimensional surface, we obtain a two-dimensional Poincaré surface of section (SOS). The SOS can be used to define a two-dimensional return map ($\mathbb{R}^2 \to \mathbb{R}^2$) for a constant energy, E and given by

$$U^{-}_{xp_x} = \Big\{ (x, y, p_x, p_y) \in \mathbb{R}^4 \mid y = y_w = 1/\sqrt{2}, \\ p_y(x, y, p_x; E) < 0 \Big\}, \tag{12}$$

where $p_y < 0$ enforces a directional crossing of the surface and in this case, trajectories with $y-$momentum directed towards the bottom well.

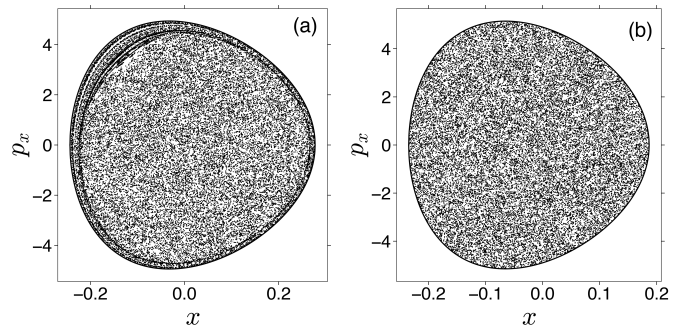

Fig. 2 Poincaré surface of section of the trajectories crossing the surface (12) for the parameters (a) $\zeta = 1.00, \lambda = 1.50$ (b) $\zeta = 2.30, \lambda = 1.95$ at total energy $E = 1.5$. While the range and coupling parameter shown in (a) exhibits a combination of regular and chaotic behavior, the set of parameters used for (b) is almost completely chaotic.

In Fig. 2, we show the Poincaré section of trajectories initialized on the surface (12) and integrated for 10^3 time units (for the chosen parameters, the barrier frequency is $\omega_b = \sqrt{(4\mathscr{V}^{\ddagger})/(y_w^2 m_y)} = 1.0$). The trajectories are sampled on the energy surface $E = 1.5$ which is above the critical energy and for the two sets of system parameters. The Poincaré sections show that the phase space of the system dynamics for $\zeta = 1.00, \lambda = 1.50$ is a combination of regular and chaotic motion as indicated by the KAM islands near the edge of the energy boundary's intersection with the surface and the sea surrounding these islands, respectively. For the parameters $\zeta = 2.30, \lambda = 1.95$, the surface lacks any regular motion since the KAM islands are absent. Thus, while the first set of coupling and range parameters exhibits a combination of chaotic and regular motion, the second set of parameters exhibits completely chaotic motion, respectively. As has been discussed in the literature[26,27], these two types of global dynamics are typical of molecular systems that undergo isomerization. However, inferring about the phase space mechanism of the isomerization, that is *how and which trajectories lead to reaction*, requires further local analysis (linearization) around fixed points in the Poincaré return map for finding the periodic orbit and its stable and unstable manifolds[28–30]. Furthermore, as the dimension of the phase space increases due to the coupling with bath modes, trajectories in more than four-dimensional phase space will intersect the two dimensional surface with probability close to zero, and hence the Poincaré return map constructed using a two-dimensional surface of section can not catch trajectories with dynamically different fates. For the parameters chosen here, the integration time can be considered as "long" compared to the time scale involved in the barrier crossings and can become infeasible for high dimensional phase space, while at the same time we do not gain much understanding of the hierarchy (time ordering) of reactive trajectories using Poincaré sections. To address this issue, we will present a direct construction of the so called *reactive islands*[4,26,28,30], and a simple trajectory diagnostic method, Lagrangian descriptor contour map, that can detect the phase space structures in the system Hamiltonian. In addition, the Lagrangian descriptor (LD) contour map obtained using either the formulation (49) or (53) can reveal the reaction mechanism by detecting the reactive island structures in high dimensional phase space of a system-bath Hamiltonian. However, before proceeding to the system-bath Hamiltonian, we will verify the reactive islands obtained using the LD contour map by comparing with the *direct construction* of the reactive islands in the system Hamiltonian.

3.1.1 Direct construction of reactive islands

Here we discuss the computational approach for directly obtaining the reactive islands for the two degrees of freedom De Leon-Berne Hamiltonian (2) presented in the Appendix B. The procedure relies on the linearization around the index-1 saddle equilibrium point and the corresponding eigenvalue problem yields the eigenvectors in the center manifold which is used to generate initial conditions for the unstable periodic orbit. Since computing unstable periodic orbits is a fundamental step in studying transport across index-1 saddle, we have made this step available as an open source python package which also includes the De Leon-Berne Hamiltonian as an example[78]. Next, the eigenvectors that span the unstable and stable subspace at the index-1 saddle equi-

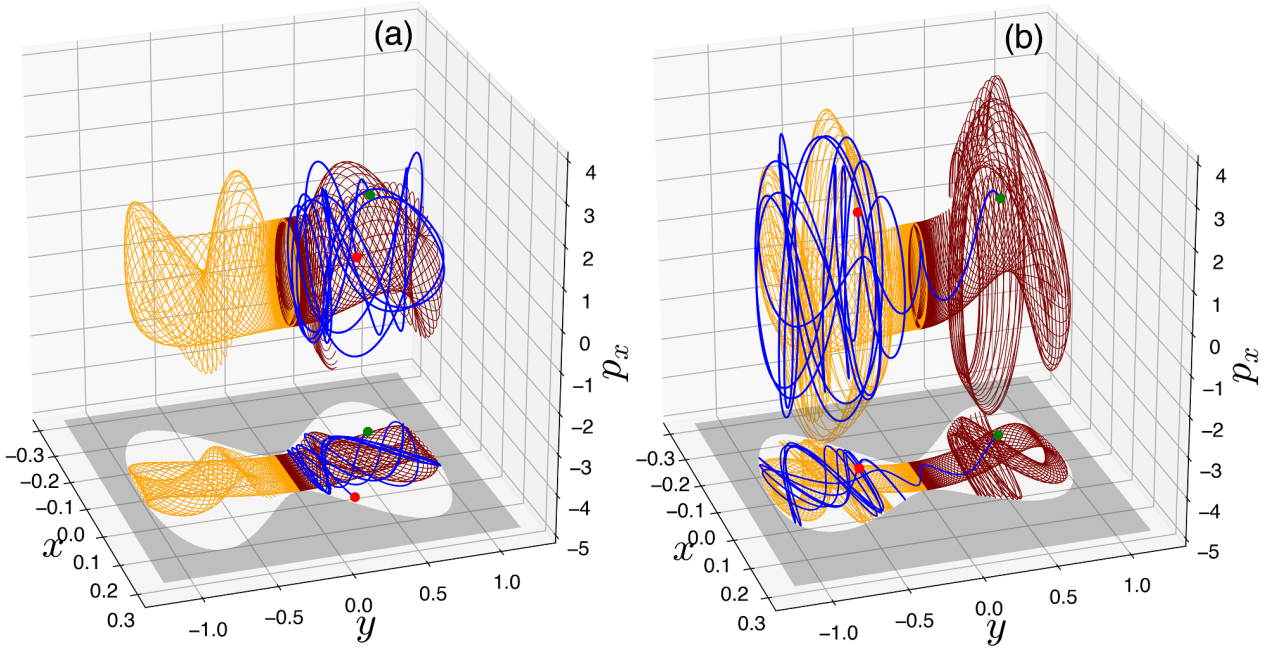

Fig. 3 Phase space and configuration space view. Shows the cylindrical (tube) invariant manifolds of the unstable periodic orbit associated with the index-1 saddle equilibrium point in the bottleneck for the total energy, $E = 1.1$, and for (a) $\zeta = 1.00, \lambda = 1.50$ (b) $\zeta = 2.30, \lambda = 1.95$. The Hill's region (defined in Appendix A) for the same total energy is shown as the grey region in the configuration space. The stable and unstable manifolds in the top and bottom wells are shown as the surface with maroon and orange)= trajectories, respectively, and are obtained using numerical globalization (see Appendix B). The unstable manifold in the top well and the stable manifold in the bottom well are not shown here, to avoid cluttering the figure. The example trajectory (shown in blue with green and red circles marking the start and end coordinates) with configuration coordinates $(-0.1, 1/\sqrt{2}, 1.0, p_y(E;(\zeta,\lambda)))$ integrated for 30 time units for both the set of system parameters. During this time interval, the trajectory crosses the barrier (for $\zeta = 2.30, \lambda = 1.95$) by entering the stable manifold in the top well, crossing the bottleneck, and then entering the unstable manifold in the bottom well. The trajectory is trapped in the well as long as it remains on the outside the manifolds.

librium point are placed on the unstable periodic orbit to generate initial conditions which are then integrated to construct the *global* stable and unstable invariant manifolds of the unstable periodic orbit associated with an index-1 saddle. As pointed out in the introduction, these invariant manifolds are two-dimensional on the three-dimensional energy surface making them codimension-1 on the energy surface, and have cylindrical geometry, that is $\mathbb{R}^1 \times \mathbb{S}^1$, and hence are also called *tubes*. Thus, they are of appropriate dimension to partition the energy surface in four dimensional phase space and thus mediate trajectories that cross the barrier[3] between the isomer wells. Since the trajectories that cross the barrier must enter the stable manifold of the unstable periodic orbit, cross the bottleneck of the energy surface, and then enter the unstable manifold of the unstable periodic orbit (projection of the unstable periodic orbit on the configuration space is referred to as the transition state) associated with the index-1 saddle equilibrium point in the bottleneck. For example, if we define the forward reaction as going from the top to the bottom well, then forward reactive trajectories must pass through the stable manifold's branch (denoted by the surface with cyan trajectories in Fig. 3) in the top well, cross the unstable periodic orbit in the bottleneck, and enter the bottom well through the unstable manifold's branch (denoted by the surface with orange trajectories in Fig. 3) in the bottom well. An example trajectory (shown as the blue curve with green and red circles denoting initial and final phase space coordinates) that undergoes reaction by passing through the cylindrical manifolds is shown in Fig. 3.

Reactive islands in the two degrees of freedom system are the intersection of the tube manifolds with a two-dimensional surface in the three-dimensional energy surface which makes the reactive islands one-dimensional. Depending on the geometry of the globalized tube manifolds and the choice of the two-dimensional surface, the intersection of the invariant manifolds can be either closed curves or non-closed as has been known in the literature[67,79]. Patra and Keshavamurthy[63] have discussed the role of reactive islands in sampling reactive trajectories which can be thought of as rare events when a trapped trajectory in a system-bath model crosses the potential energy barrier. This observation has also been experimentally validated[80] where the reaction probability (or transition probability) for a given total energy can be calculated directly as the area of the reactive islands relative to the area of the energetically accessible region on the surface. This quantitative approach based on reactive island areas has been used to develop the reactive island kinetic theory of reaction rates[30,67].

It follows from the construction of the cylindrical manifolds that the trajectories on the stable manifold approach the unstable periodic orbit in the bottleneck in forward time which implies that a trajectory exiting the top well has to appear inside the *first intersection* (in backward time) of the stable manifold with the surface (12). A similar justification holds for the *first intersection* (in forward time) of the unstable manifold for a trajectory enter-

ing the bottom well. Thus, the first intersections of the stable and unstable manifolds define the reactive islands of imminent reactions. So given the phase space coordinates of a trajectory inside these reactive islands we can specify the upper bound of the barrier crossing time by the average time taken by the trajectories on the manifold to intersect the surface. Furthermore, the pre-image and image of these first intersections of the stable and unstable manifolds, respectively, can be used to construct an itinerary of the reactive trajectory in the molecular phase space[5,81,82]. It is to be noted that this requires densifying the pre-image and image curves to generate smooth approximations[83,84] for the area calculations to be of practical interest. Here, we present the qualitative changes in the reactive islands for the two sets of the parameters in the system dynamics at three different energies.

In Fig. 4 and 5, we show the reactive islands (as orange and maroon curves) in the top well constructed from the intersections of the globalized unstable (orange) and stable (maroon) cylindrical manifolds with the surface (12). The top row in both figures shows the intersections of the unstable manifolds of the unstable periodic orbit at the total energy, $E = 1.5$, with the surface for $\tau = 30$ and the bottom row shows the same for the stable manifolds. We note here that for the parameters considered here (which affects the geometry of the cylindrical manifolds as is evident in Fig. 3) and the choice of the surface (12), only the reactive islands of imminent reactions are closed curves and their pre-images and images are non-closed curves. A detailed geometric analysis of these intersections requires careful discussion of the tube dynamics and is beyond the scope of this study but can be found elsewhere[81,84,85].

3.1.2 Detecting the hierarchy of reactive islands using Lagrangian descriptors

In a recent work[75,76], we showed that the singular features in the Lagrangian descriptors (LD) identify the normally hyperbolic invariant manifold and its unstable and stable manifolds in two and three degrees of freedom (for both linear and nonlinear) Hamiltonian systems. We also compared the fixed (49) and variable (53) integration time formulation for the two and three degrees-of-freedom system with Hénon-Heiles type potential. Since the reactive islands are the interior of the intersections of the unstable and stable invariant manifolds with the surface, such as defined by the Eqn. (12), it is reasonable to check that the singular features in the Lagrangian descriptor contour maps can reveal the reactive island structures. To this end, it has been shown that for the Müller-Brown potential energy surface and De Leon-Berne Hamiltonian Lagrangian descriptor contour maps can reveal the hierarchy of reactive islands[5,63]. The hierarchy is formed when the first intersection of the stable manifold is evolved backwards in time to give the *pre-image* and the first intersection of the unstable manifold is evolved forward in time to give the *image* of the reactive island of imminent reaction. It is to be noted that the reactive islands formed by the stable manifold in the top well mediates the forward reactive trajectories going to the bottom well. Similarly, the reactive islands formed by the unstable manifold in the top well mediates the backward reactive trajectories coming from the bottom well. Thus, the knowledge of the reactive island structures on the surface (12) shows the phase space mechanism of the reaction as defined for the potential energy surface (14).

Now, we establish the connection between the hierarchy of the reactive islands generated by the globalized invariant manifolds. This globalization implies that the intersection of these invariant manifolds with the surface has a natural time ordering which produces the hierarchy in the reactive island structure starting from the first intersections of the unstable and stable manifolds. Furthermore, this hierarchy can be used to explain the temporal features in the committor probability[66,86] of a set of initial conditions which are specified by fixing position coordinates (configurations) and selecting momenta to satisfy the fixed energy constraint. First, we verify the approach of using LD contour maps for detecting reactive islands by comparing the direct numerical construction in §:3.1.1 with the singular features in the LD plots.

In Figs. 4(a,c) and 5(a,c), we show the fixed integration time LD contour maps for the two sets of the system parameters and where the singular features as indicated by the one-dimensional sections in the respective (b,d) line plots. Even though, the singular features in the contour maps agree with the directly constructed reactive islands, the fixed integration time LD has a large number of minima that are generated due to trapped trajectories outside the invariant manifolds. Due to these "ripples" in the function M values, we resort to calculating the variable integration time LD using $\tau^{\pm} = 30$ in the formulation (53). This is shown in Figs. 6(d,f) and 7(d,f) for the two sets of the parameters, respectively.

In Fig. 6(b,c) and 7(b,c), we show the committor probabilities of the five sets of initial conditions for the two sets of parameters initialized on the surface (12). The committor probabilities show the step jumps resulting from the initial conditions inside the reactive islands that lead to the bottom well while the flat portions of the committor corresponds to the trapping in the well. The drop in the committor corresponds to the recrossings which is related to the reactive island structure that leads to the top well from the bottom well (called as backward reaction[67]). Thus, the reactive islands leading to forward reaction is revealed by forward time LD since the blue set of initial conditions react immediately in forward time (~ 5 time units) and take longer to react in backward time (~ 20 time units).

The finer structure in the interior of the reactive islands is absent in these maps because the integration is terminated once the trajectory satisfies the product criterion and hence they only appear in the fixed integration time LD as shown in Figs. 4 and 5. These finer structures are to be expected due to the global recrossings of the barrier on a bounded energy surface and are suppressed when using the variable integration time (cf. Fig. 6 (b,c) and Fig. 4 (a,d)) formulation. Besides, the formula (53) is faster to compute compared to the fixed integration time formula (49) in a high-dimensional phase space, and hence is more suitable for setting up seed initial conditions for harvesting reactive trajectories in transition path sampling.

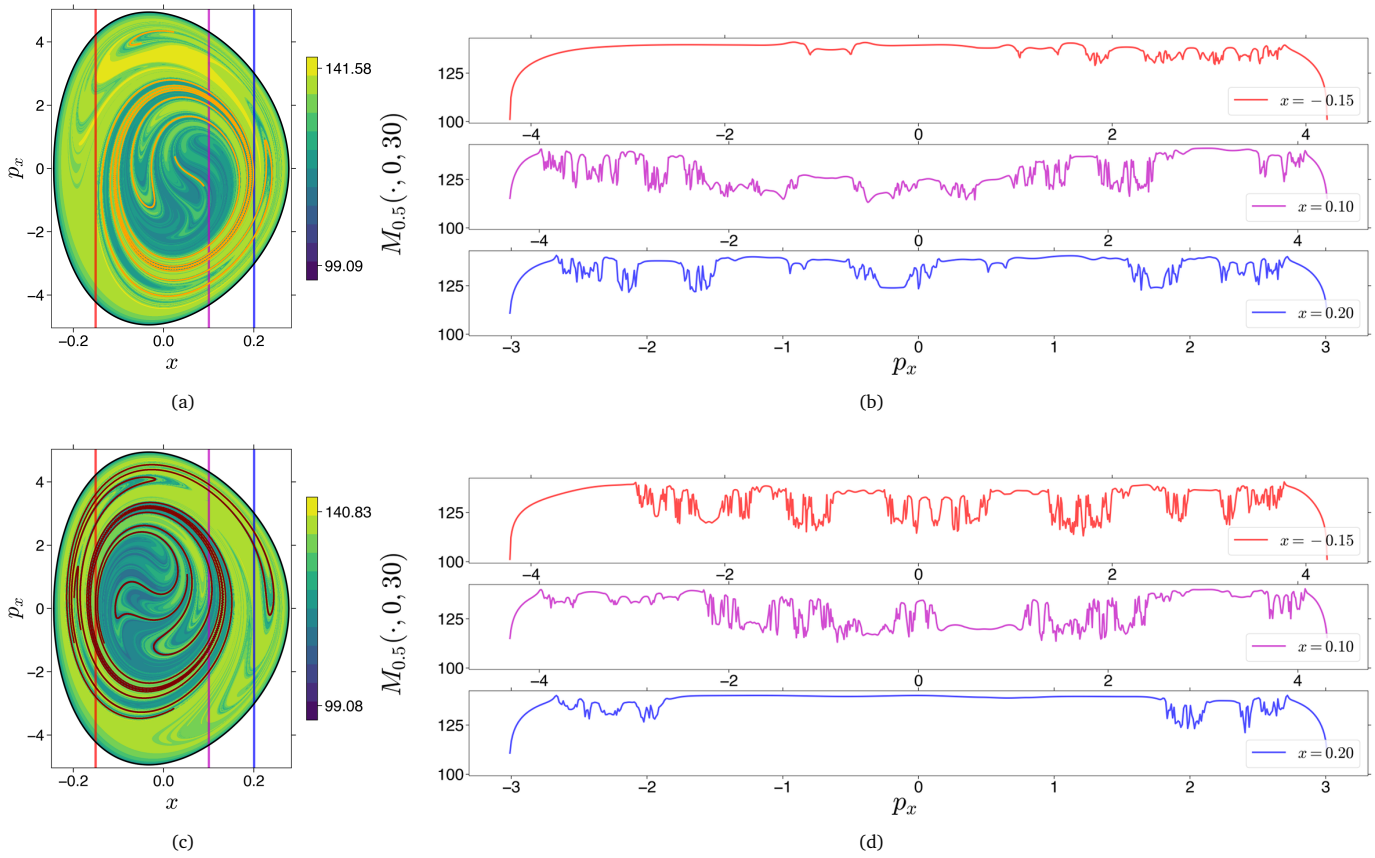

Fig. 4 Reactive islands and Lagrangian descriptors for the system model. The singular features in the contour maps identify the reactive islands (in orange and maroon curves) for $\zeta = 1.00$ and $\lambda = 1.50$ at total energy $E = 1.500$. (a) shows the fixed integration time backward LD and (b) shows the fixed integration time forward LD for $\tau = 30$. In both the contour maps, the orange and maroon curves denote the intersection of unstable and stable manifolds with the surface (12), respectively, and are computed directly by globalizing the manifolds for 30 time units and recording their intersections with the surface. (c) and (d) show the function M value, $M_{0.5}(\cdot, 0, 30)$, for the initial conditions along the constant $x-$coordinate.

3.2 System-bath dynamics

Now, we will use the LD contour maps to identify reactive islands in the system-bath model with $N_S(N_B+1)$ degrees of freedom. Since the system dynamics for the isomerization is modelled by the De Leon-Berne Hamiltonian ($N_S = 2$) and coupled with $N_B = 64$ harmonic oscillators, the configuration space is 130-dimensional and as a result 260-dimensional phase space. However, since the isomerization model involves the two coordinates (x, y) in the system-bath model (8), a two-dimensional surface with either (x, p_x) or (y, p_y) as the coordinates becomes an appropriate choice for finding the reactive islands. In the $2N_S(N_B+1)$-dimensional phase space, we consider the isoenergetic two-dimensional surface given by

$$U^{-}_{xp_x} = \Big\{ (x, y, \mathbf{x}, \mathbf{y}, p_x, p_y, \mathbf{p_x}, \mathbf{p_y}) \in \mathbb{R}^{2N_S(N_B+1)} \mid y = y_w, \mathbf{x} = 0, \mathbf{y} = 0, \mathbf{p_x} = 0, \mathbf{p_y} = 0, p_y(\cdot; E) < 0 \Big\}. \quad (13)$$

The negative p_y enforces a directional crossing such that we only record trajectories with $y-$momentum pointing towards the bottom well. On this surface, we initialize a microcanonical ensemble at $E = 1.5$, and integrate them for 30 time units in forward and backward or until their $y-$coordinate is within tolerance (10^{-6}) of the condition, $y_w = -1/\sqrt{2}$. The terminal condition corresponds to the formation of a product while the resulting LD computation becomes a variable time formulation (53). In what follows, we use the bath parameters $m_i = 1.0, \omega_c = \sqrt{5} \approx 2.236, \eta_x = \eta_y = 0.1$ which represents a weak coupling of the bath modes (for $m_s = 8.0, \omega_b = 1.0, \Delta E = 0.5, \varepsilon_s = 1.0$, we get $\eta_x/(m_s\omega_b) < \Delta E/\varepsilon_s$) and thus, acts as perturbation to the dynamics given by the system Hamiltonian. Here, we note that in a recent work the influence of the solvent's mass (in particular the timescale mismatch between a solute and solvent's motion) on the phase space dividing surface has been illustrated using a Lennard-Jones like repulsion term[87,88].

3.2.1 Detecting the hierarchy of reactive islands using Lagrangian descriptors

In Fig. 8(a,c) and Fig. 9(a,c), we show the backward and forward variable integration time (defined by the Eqn. (53) with $\tau^{\pm} = 30$) LD contour maps along with one-dimensional sections at constant $x-$coordinate. In both cases of the system parameters, we observe that the singular features in the variable integration time LD contour maps identify the boundaries of the reactive islands and the flat regions between the singular points identify the interior of

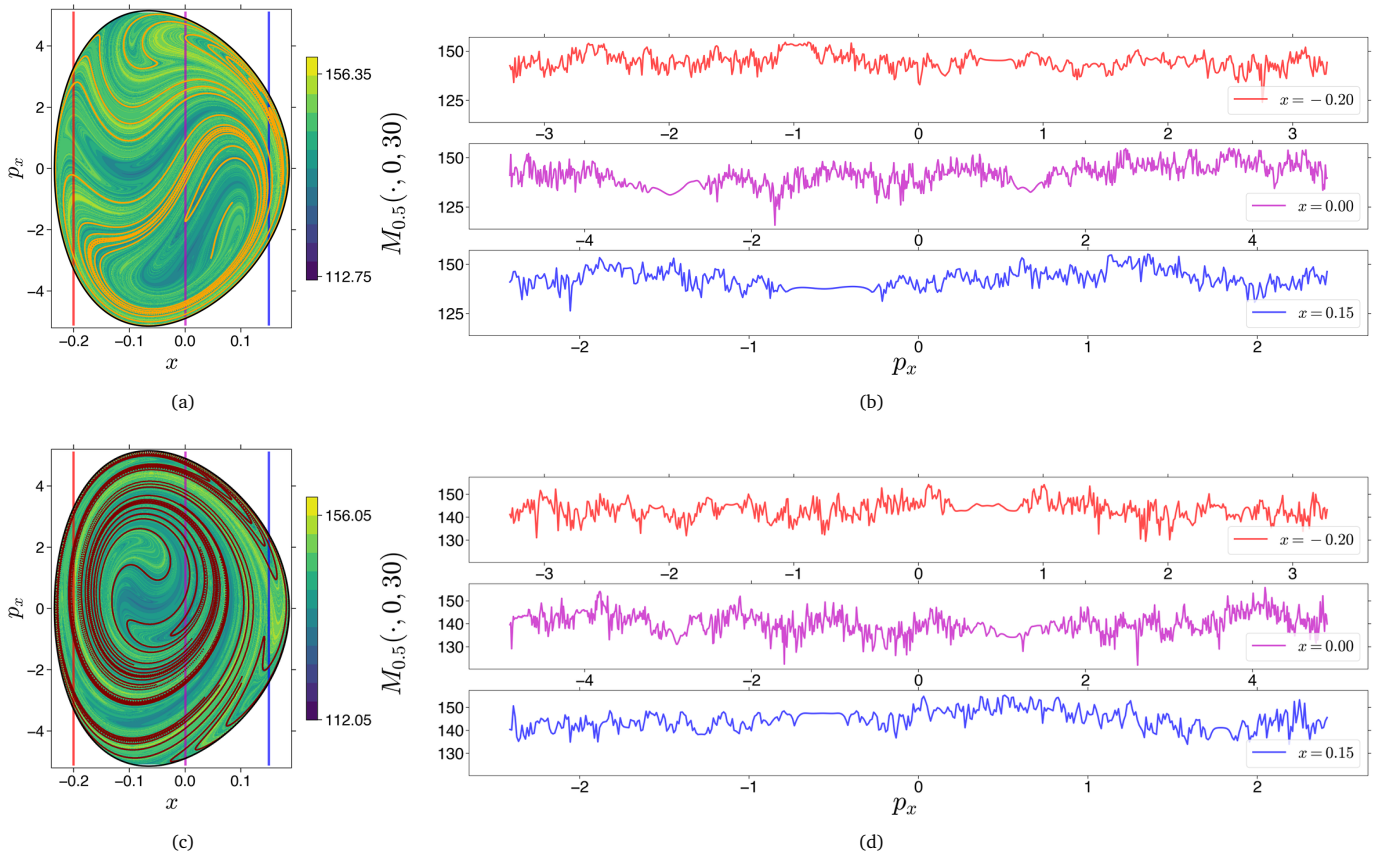

Fig. 5 Reactive islands and Lagrangian descriptors for the system model. The singular features in the contour maps identify the reactive islands (in orange and maroon curves) for $\zeta = 2.30$ and $\lambda = 1.95$ at total energy $E = 1.500$. (a) shows the fixed integration time backward LD and (b) shows the fixed integration time forward LD for $\tau = 30$. In both the contour maps, the orange and maroon curves denote the intersection of unstable and stable manifolds with the surface (12), respectively, and are computed directly by globalizing the manifolds for 30 time units and recording their intersections with the surface. (c) and (d) show the function M value, $M_{0.5}(\cdot, 0, 30)$, for the initial conditions along the constant $x-$coordinate.

these reactive islands[76].

Using the integration time of $\tau = \pm 30$, we observe that the reactive islands of imminent reactions have appeared in both cases of the system parameters at the total energy, $E = 1.5$. Furthermore, in Figs. 8(a,c) and 9(a,c), we observe the appearance of higher order reactive islands which manifest as singular features narrow flat regions in the one-dimensional sections. These higher order reactive islands also explain why even a small variation in the $x-$ momentum can cause reaction to be delayed as the initial condition has to pass through the hierarchy of reactive islands to cross the barrier. Comparing the Fig. 6(d,f) with Fig. 8(a,c) which are for the same system parameters: $\zeta = 1.00, \lambda = 1.50$, we observe that the reactive island structures are not destroyed by a light bath. This observation is corroborated when the system parameters are changed to $\zeta = 2.30, \lambda = 1.95$ (cf. Figs. 7(d,f) and 9(a,c)). Even though, the reactive island structures in the system model are now different, the reactive islands still persist. Our numerical experiments at higher energies also supports this observation. Thus we can conclude that the gross picture of the phase space structures in the system dynamics is not destroyed even though individual configurations show distinctly different dynamics as picked up by the committor probabilities in Figs. 8(e) and 9(e). This has two potential implications: firstly, the global dynamics can be diagnosed using Lagrangian descriptors which detect the reactive islands and secondly, once the skeleton of the global behaviour is revealed, specific configurations can be initialized in a systematic way in the high-dimensional phase space to find all the reactive trajectories used for rate calculations.

4 Conclusion and outlook

The role of reactive islands in two degrees of freedom isomerization dynamics has been known since the work of De Leon, Marston, Davis[1–4]. Theoretical developments have shown their role in the qualitative understanding of reaction pathways and their usefulness in computing reaction rates. In this article, we have presented a computational approach of combining reactive islands, Lagrangian descriptors, and committor probabilities for identifying the phase space structures that govern reaction dynamics in a system-bath model. We have shown a *direct approach* for obtaining the reactive islands by computing the cylindrical invariant manifolds (tubes) in a well-known two degrees of freedom model of isomerization, De Leon-Berne Hamiltonian[26,27]. Then, we have verified the Lagrangian descriptor method for identifying reactive islands and their hierarchy[5] in the two degrees of freedom system. We have used this approach in a high dimensional system-bath model where reactive islands were ob-

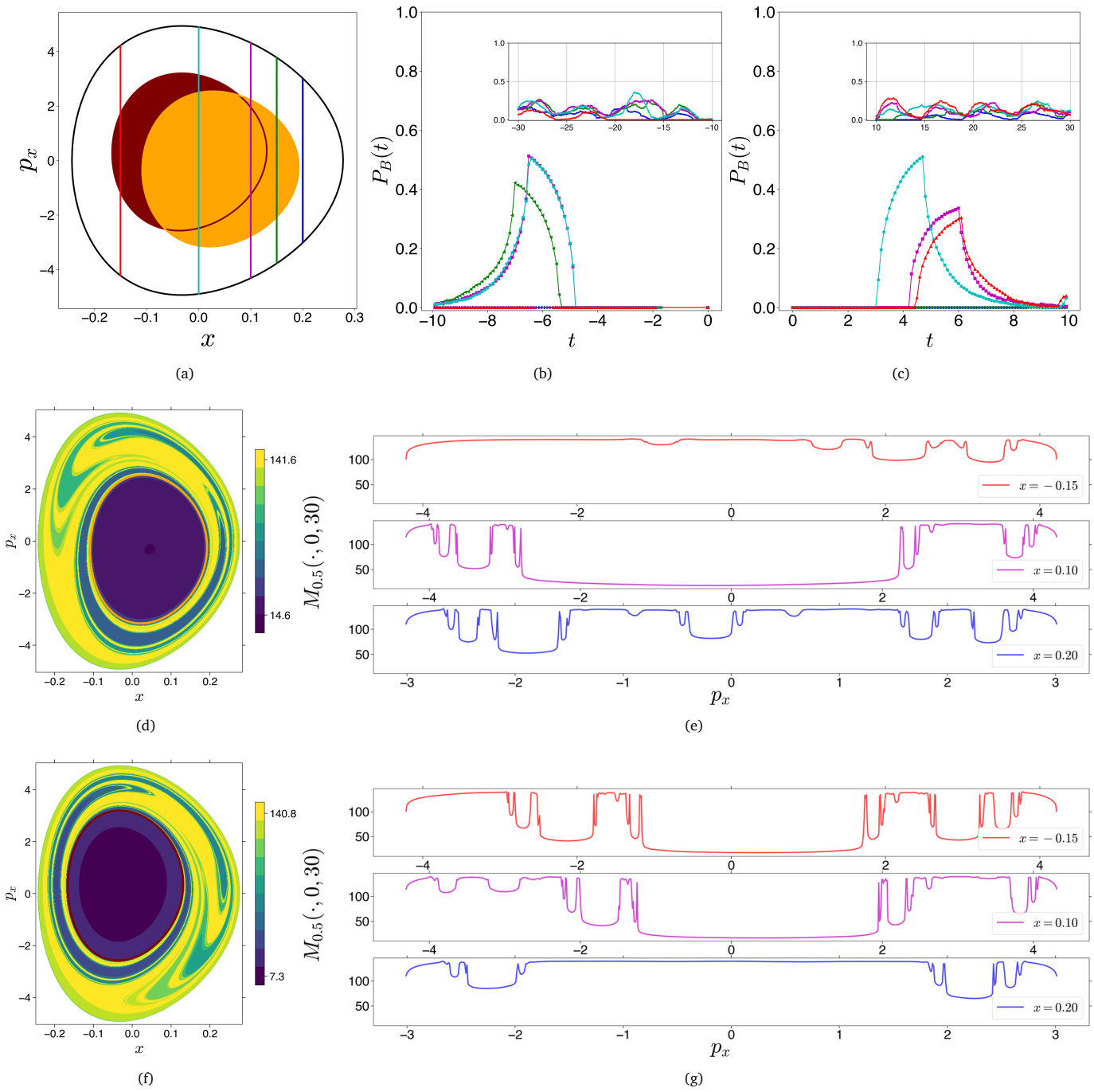

Fig. 6 Committor probabilities and reactive islands in the system model. Shows the reactive islands are identified by the singular features in the LD contour maps for parameters: $\zeta = 1.00$, $\lambda = 1.50$ at total energy $E = 1.500$. (a) Shows the configurations used for committor probability calculations. (b,c) Show the committor probabilities of the five configurations for the backward and forward reaction, respectively, for $\tau = 30$ time units. (d,f) Show the variable integration time backward and forward LD, respectively, and (e,g) show the function M value, $M_{0.5}(\cdot, 0, 30)$, for the initial conditions along the three configurations at constant $x-$coordinate.

tained and checked using committor probabilities of configurations initialized in the isomer well A. The hierarchy of the reactive islands explain the phase space mechanism of a solvent's influence on the isomerization and the barrier recrossings associated with solution-phase reactions.

In this study, we observed that the phase space structure of reactive islands that contain the global behaviour of trajectories is preserved when a molecule undergoes isomerization in a light bath (mass of the solvent molecules is less than the mass of the molecule). This is verified by the committor probabilities of a few test configurations which also reveal the barrier recrossings due to a solvent [19,20]. This indicates that the *reactive islands persist* even when the isomerization reaction takes place in a low viscosity solvent. This observation is also in accordance with what has been

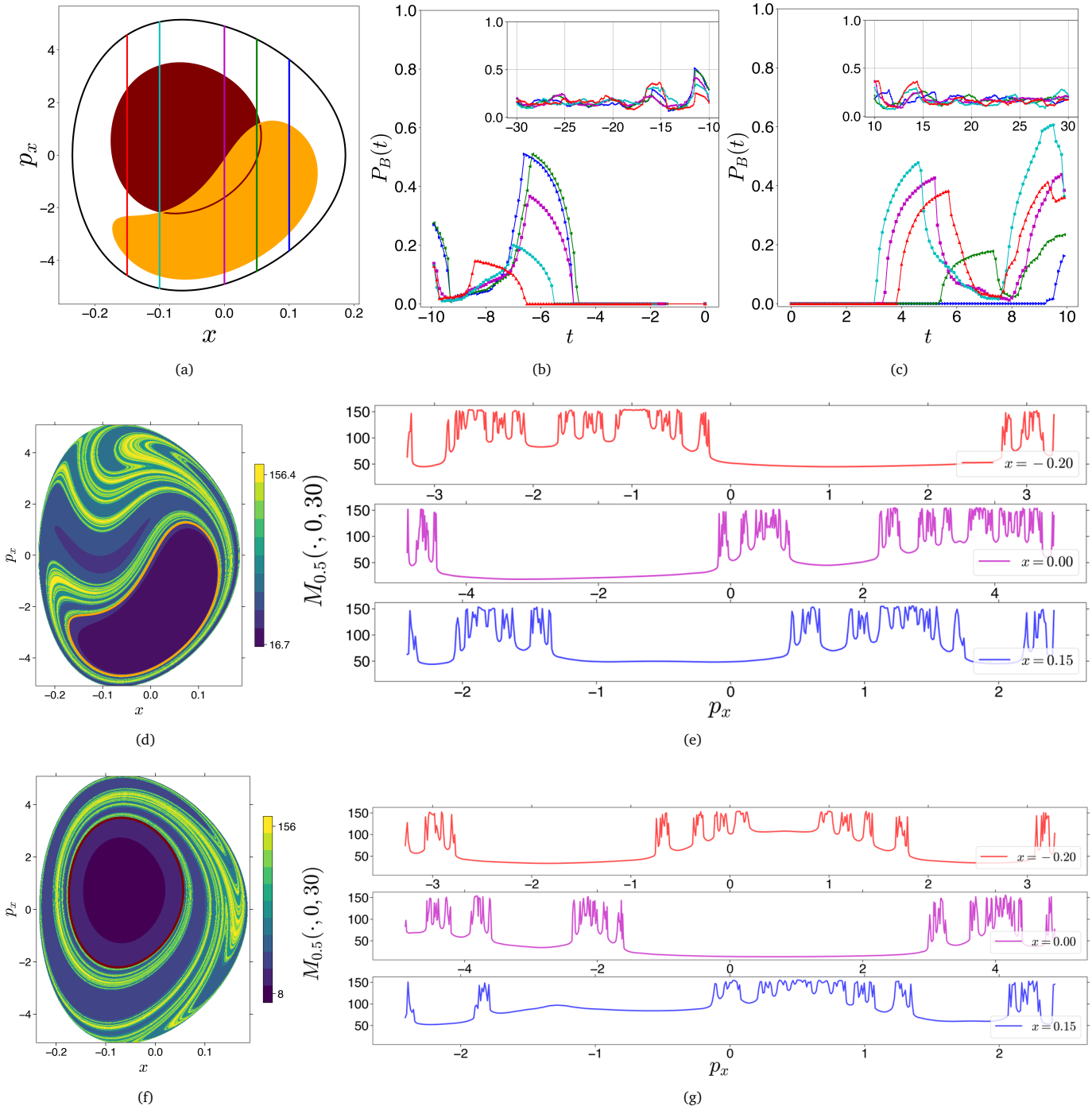

Fig. 7 Committor probabilities and reactive islands in the system model. Shows the reactive islands are identified by the singular features in the LD contour maps for parameters: $\zeta = 2.30$, $\lambda = 1.95$ at total energy $E = 1.500$. (a) Shows the configurations used for committor probability calculations. (b,c) Show the committor probabilities of the five configurations for the backward and forward reaction, respectively, for $\tau = 30$ time units. (d,f) Show the variable integration time backward and forward LD, respectively, and (e,g) show the function M value, $M_{0.5}(\cdot, 0, 30)$, for the initial conditions along the three configurations at constant $x-$coordinate.

thought of as cylindrical manifolds becoming *fuzzy cylinders*[5] in the presence of random forces[89]. The connection between phase space structures in system-bath Hamiltonian and reactions in solvent modelled by Langevin dynamics[22,90,91] remains to be made, and related future work will be along this direction. Furthermore, the robustness of the reactive islands to parameters of the solvent remains to be investigated. This includes the influence of the mass, frequency dependent friction[92], and cut-off frequency on the reactive islands for a given system dynamics. Understanding the effects of these solvent parameters on the reactive islands will provide insights into the phase space mechanism of reactions in a solvent and aid transition path sampling methods for calculating

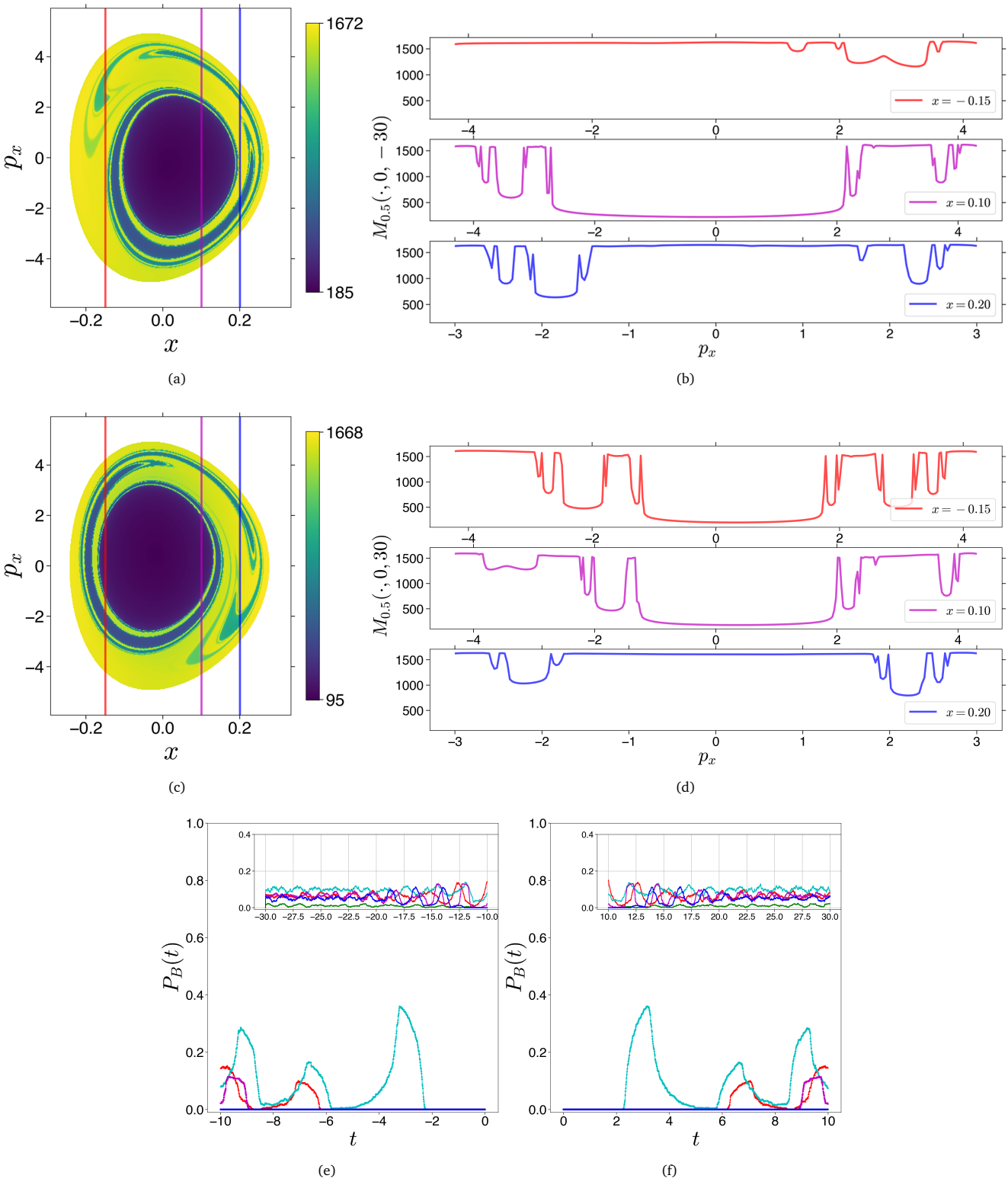

Fig. 8 Committor probabilities and reactive islands in the system-bath model for parameters: $\zeta = 1.00, \lambda = 1.50$ and at total energy $E = 1.5$. The color map shows the variable integration time forward LD for (a, c) $\tau = 30$ computed on the surface (13). One dimensional sections along constant x-coordinate is shown in (b, d) for the three configurations of the system coordinates. (e,f) Show the committor probabilities for the same initial configuration of the system as in the Fig. 6(a).

reaction rates when the solvent is altered for a given reaction.

Conflicts of interest

There are no conflicts of interest to declare.

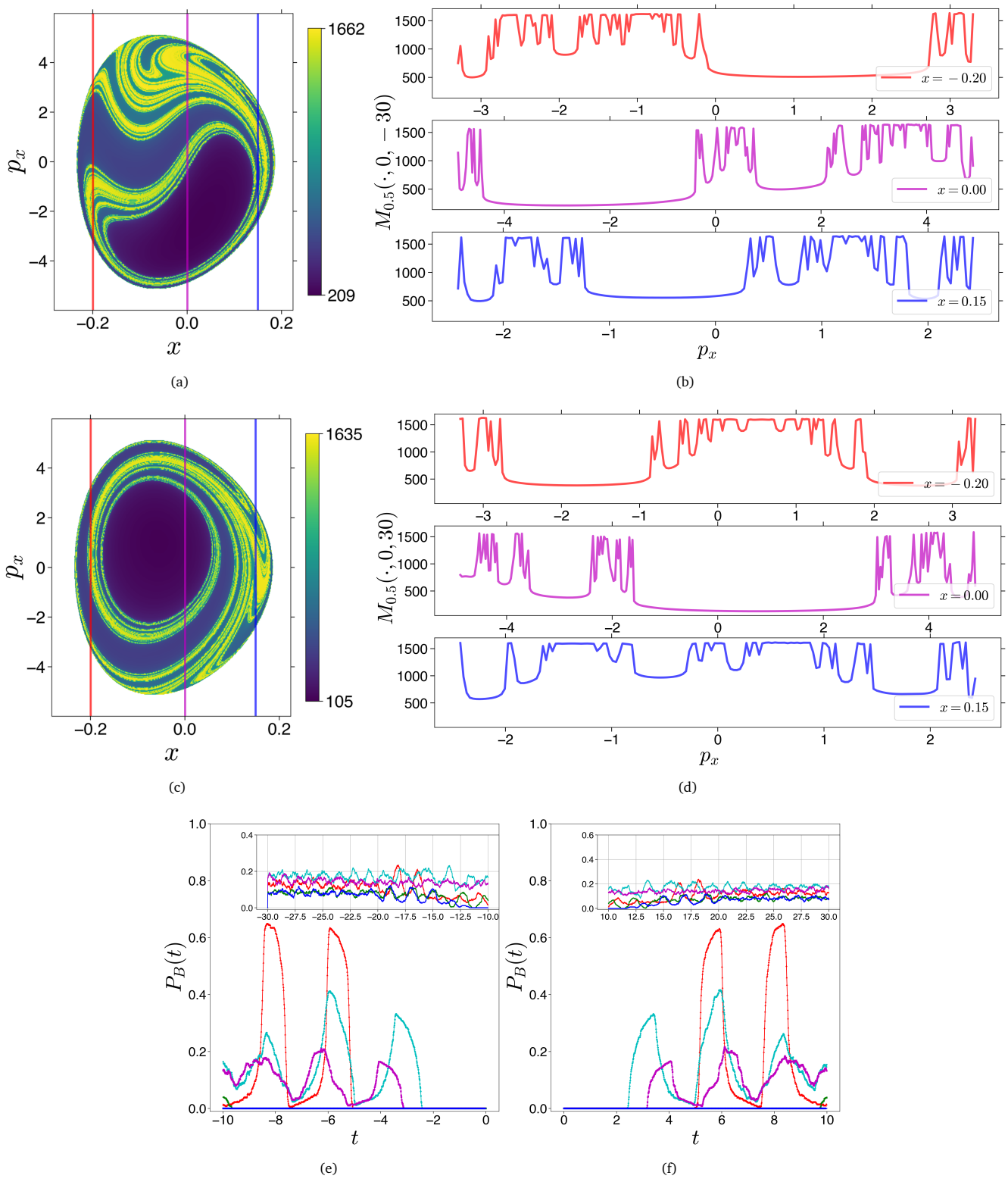

Fig. 9 Committor probabilities and reactive islands in the system-bath model for parameters: $\zeta = 2.30, \lambda = 1.95$ and at total energy $E = 1.5$. The color map shows the variable integration time forward LD for (a, c) $\tau = 30$ computed on the surface (13). One dimensional sections along constant x-coordinate is shown in (b, d) for the three configurations of the system coordinates. (e,f) Show the committor probabilities for the same initial configuration of the system as in the Fig. 7 (a).

Acknowledgements

We acknowledge the support of EPSRC Grant No. EP/P021123/1 and Office of Naval Research Grant No. N00014-01-1-0769. We also acknowledge the high performance computing cluster of Linux servers, CREAM, at the School of Mathematics for sup-

porting the computational needs of this work. The authors acknowledge critical discussions and feedback from Srihari Keshavamurthy on a draft of this article.

References

1 M. J. Davis, *The Journal of Chemical Physics*, 1985, **83**, 1016–1031.
2 M. J. Davis, *The Journal of Chemical Physics*, 1987, **86**, 3978–4003.
3 C. C. Marston and N. De Leon, *The Journal of Chemical Physics*, 1989, **91**, 3392–3404.
4 N. De Leon and C. C. Marston, *The Journal of Chemical Physics*, 1989, **91**, 3405–3425.
5 S. Patra and S. Keshavamurthy, *Physical Chemistry Chemical Physics*, 2018, **20**, 4970–4981.
6 G. M. Wieder and R. A. Marcus, *The Journal of Chemical Physics*, 1962, **37**, 1835–1852.
7 J. W. McIver and A. Komornicki, *Journal of the American Chemical Society*, 1972, **94**, 2625–2633.
8 C. Dugave and L. Demange, *Chemical Reviews*, 2003, **103**, 2475–2532.
9 T. Donohoe, T. O'Riordan and C. Rosa, *Angewandte Chemie International Edition*, 2009, **48**, 1014–1017.
10 C. C. Price and W. H. Snyder, *Journal of the American Chemical Society*, 1961, **83**, 1773–1773.
11 T. Halicioğlu and O. Sinanoğlu, *Annals of the New York Academy of Sciences*, 1969, **158**, 308–317.
12 S. R. Flom, V. Nagarajan and P. F. Barbara, *The Journal of Physical Chemistry*, 1986, **90**, 2085–2092.
13 E. S. Eberhardt, S. N. Loh, A. P. Hinck and R. T. Raines, *Journal of the American Chemical Society*, 1992, **114**, 5437–5439.
14 E. M. Duffy, D. L. Severance and W. L. Jorgensen, *Journal of the American Chemical Society*, 1992, **114**, 7535–7542.
15 R. Zwanzig, *Journal of Statistical Physics*, 1973, **9**, 215–220.
16 H. Kramers, *Physica*, 1940, **7**, 284–304.
17 V. I. Mel'nikov and S. V. Meshkov, *The Journal of Chemical Physics*, 1986, **85**, 1018–1027.
18 E. Pollak, H. Grabert and P. Hänggi, *The Journal of chemical physics*, 1989, **91**, 4073–4087.
19 E. Pollak and P. Talkner, *Physical Review E*, 1995, **51**, 1868–1878.
20 E. Pollak, *J. Chem. Phys.*, 1986, **85**, 865–867.
21 E. Pollak and P. Talkner, *Chaos: An Interdisciplinary Journal of Nonlinear Science*, 2005, **15**, 026116.
22 E. Cortés, B. J. West and K. Lindenberg, *The Journal of Chemical Physics*, 1985, **82**, 2708–2717.
23 S. C. Tucker, *The Journal of Physical Chemistry*, 1993, **97**, 1596–1609.
24 S. C. Tucker, *The Journal of Chemical Physics*, 1994, **101**, 2006–2015.
25 S. C. Tucker, *Theoretical Chemistry Accounts: Theory, Computation, and Modeling (Theoretica Chimica Acta)*, 2000, **103**, 209–211.
26 N. De Leon and B. J. Berne, *The Journal of Chemical Physics*, 1981, **75**, 3495–3510.
27 B. J. Berne, N. De Leon and R. O. Rosenberg, *The Journal of Physical Chemistry*, 1982, **86**, 2166–2177.
28 N. De Leon, M. A. Mehta and R. Q. Topper, *The Journal of Chemical Physics*, 1991, **94**, 8310–8328.
29 N. De Leon, M. A. Mehta and R. Q. Topper, *The Journal of Chemical Physics*, 1991, **94**, 8329–8341.
30 N. De Leon, *The Journal of Chemical Physics*, 1992, **96**, 285–297.
31 D. Wales, *Energy Landscapes: Applications to Clusters, Biomolecules and Glasses*, Cambridge University Press, 2004.
32 S. Wiggins, L. Wiesenfeld, C. Jaffé and T. Uzer, *Physical Review Letters*, 2001, **86**, 5478–5481.
33 T. Uzer, C. Jaffé, J. Palacián, P. Yanguas and S. Wiggins, *Nonlinearity*, 2002, **15**, 957–992.
34 H. Waalkens and S. Wiggins, *J. Phys. A: Math. Gen.*, 2004, **37**, L435.
35 S. Wiggins, *Physica D*, 1990, **44**, 471–501.
36 S. Wiggins, *Normally hyperbolic invariant manifolds in dynamical systems*, Springer Science & Business Media, 2013, vol. 105.
37 P. Pechukas and F. J. McLafferty, *J. Chem. Phys.*, 1973, **58**, 1622–1625.
38 P. Pechukas and E. Pollak, *J. Chem. Phys.*, 1977, **67**, 5976–5977.
39 E. Pollak and P. Pechukas, *J. Chem. Phys.*, 1978, **69**, 1218–1226.
40 P. Pechukas and E. Pollak, *J. Chem. Phys.*, 1979, **71**, 2062–2068.
41 R. E. Gillilan and G. S. Ezra, *J. Chem. Phys.*, 1991, **94**, 2648–2668.
42 T. Komatsuzaki and M. Nagaoka, *J. Chem. Phys.*, 1996, **105**, 10838–10848.
43 T. Komatsuzaki and M. Nagoaka, *Chem. Phys. Lett.*, 1997, **265**, 91–98.
44 T. Komatsuzaki and R. S. Berry, *J. Mol. Struct. THEOCHEM*, 2000, **506**, 55–70.
45 T. Komatsuzaki and R. S. Berry, *J. Phys. Chem. A*, 2002, **106**, 10945–10950.
46 S. Wiggins, *Regular and Chaotic Dynamics*, 2016, **21**, 621–638.
47 C. B. Li, M. Toda and T. Komatsuzaki, *J. Chem. Phys.*, 2009, **130**, 124116.
48 M. Inarrea, J. F. Palacian, A. I. Pascual and J. P. Salas, *J. Chem. Phys.*, 2011, **135**, 014110.
49 A. Allahem and T. Bartsch, *J. Chem. Phys.*, 2012, **137**, 214310.
50 F. A. L. Mauguière, P. Collins, G. S. Ezra and S. Wiggins, *International Journal of Bifurcation and Chaos*, 2013, **23**, 1330043.
51 R. S. MacKay and D. C. Strub, *Nonlinearity*, 2014, **27**, 859.
52 R. S. MacKay and D. C. Strub, *Nonlinearity*, 2015, **28**, 4303–

4329.
53 B. J. Gertner, K. R. Wilson and J. T. Hynes, *The Journal of Chemical Physics*, 1989, **90**, 3537–3558.
54 R. Q. Topper, *Reviews in Computational Chemistry*, John Wiley & Sons, Inc., Hoboken, NJ, USA, 2007, pp. 101–176.
55 M. Agaoglou, B. Aguilar-Sanjuan, V. J. García-Garrido, R. García-Meseguer, F. González-Montoya, M. Katsanikas, V. Krajňák, S. Naik and S. Wiggins, *Chemical Reactions: A Journey into Phase Space*, Zenodo v0.1.0, 2019.
56 A. M. Berezhkovskii, E. Pollak and V. Y. Zitserman, *J. Chem. Phys.*, 1992, **97**, 2422–2437.
57 E. Hershkovitz and E. Pollak, *J. Chem. Phys.*, 1997, **106**, 7678–7699.
58 S. K. Reese and S. C. Tucker, *Chemical Physics*, 1998, **235**, 171–187.
59 I. E. Craig and D. E. Manolopoulos, *J. Chem. Phys.*, 2005, **122**, 084106.
60 A. M. Mancho, S. Wiggins, J. Curbelo and C. Mendoza, *Communications in Nonlinear Science and Numerical Simulation*, 2013, **18**, 3530–3557.
61 A. Junginger and R. Hernandez, *The Journal of Physical Chemistry B*, 2016, **120**, 1720–1725.
62 A. Junginger, G. T. Craven, T. Bartsch, F. Revuelta, F. Borondo, R. Benito and R. Hernandez, *Physical Chemistry Chemical Physics*, 2016, **18**, 30270–30281.
63 S. Patra and S. Keshavamurthy, *Chemical Physics Letters*, 2015, **634**, 1–10.
64 V. Krajňák, G. S. Ezra and S. Wiggins, *International Journal of Bifurcation and Chaos*, 2020, **30**, 2050076.
65 F. González-Montoya and S. Wiggins, *Journal of Physics A: Mathematical and Theoretical*, 2020.
66 C. Dellago and P. G. Bolhuis, *Advanced Computer Simulation Approaches for Soft Matter Sciences III*, Springer, Berlin, Heidelberg, 2009, pp. 167–233.
67 A. M. Ozorio de Almeida, N. De Leon, M. A. Mehta and C. C. Marston, *Physica D: Nonlinear Phenomena*, 1990, **46**, 265 – 285.
68 J. N. Onuchic, *The Journal of Chemical Physics*, 1987, **86**, 3925–3943.
69 V. Chernyak and S. Mukamel, *The Journal of Chemical Physics*, 1996, **105**, 4565–4583.
70 A. Pomyalov and D. J. Tannor, *The Journal of Chemical Physics*, 2005, **123**, 204111.
71 A. Pereverzev, E. R. Bittner and I. Burghardt, *The Journal of Chemical Physics*, 2009, **131**, 034104.
72 L. S. Cederbaum, E. Gindensperger and I. Burghardt, *Physical Review Letters*, 2005, **94**, 113003.
73 R. Martinazzo, K. H. Hughes and I. Burghardt, *Physical Review E*, 2011, **84**, 030102.
74 C. Lopesino, F. Balibrea-Iniesta, V. J. García-Garrido, S. Wiggins and A. M. Mancho, *International Journal of Bifurcation and Chaos*, 2017, **27**, 1730001.
75 S. Naik, V. J. García-Garrido and S. Wiggins, *Communications in Nonlinear Science and Numerical Simulation*, 2019, **79**, 104907.
76 S. Naik and S. Wiggins, *Phys. Rev. E*, 2019, **100**, 022204.
77 P. G. Bolhuis, D. Chandler, C. Dellago and P. L. Geissler, *Annual Review of Physical Chemistry*, 2002, **53**, 291–318.
78 W. Lyu, S. Naik and S. Wiggins, *Journal of Open Source Software*, 2020, **5**, 1684.
79 J. Binney, O. E. Gerhard and P. Hut, *Monthly Notices of the Royal Astronomical Society*, 1985, **215**, 59–65.
80 S. D. Ross, A. E. BozorgMagham, S. Naik and L. N. Virgin, *Phys. Rev. E*, 2018, **98**, 052214.
81 W. S. Koon, M. W. Lo, J. E. Marsden and S. D. Ross, *Chaos: An Interdisciplinary Journal of Nonlinear Science*, 2000, **10**, 427–469.
82 F. Gabern, W. S. Koon, J. E. Marsden and S. D. Ross, *Physica D: Nonlinear Phenomena*, 2005, **211**, 391–406.
83 D. G. Dritschel, *Journal of Computational Physics*, 1988, **77**, 240–266.
84 S. Naik, F. Lekien and S. D. Ross, *Regular and Chaotic Dynamics*, 2017, **22**, 272–297.
85 S. Wiggins, *Introduction to Applied Nonlinear Dynamical Systems and Chaos*, Springer Science & Business Media, 2003, vol. 2.
86 C. Dellago and D. Chandler, *Bridging Time Scales: Molecular Simulations for the Next Decade*, Springer Berlin Heidelberg, Berlin, Heidelberg, 2002, vol. 605, pp. 321–333.
87 R. García-Meseguer, B. Carpenter and S. Wiggins, *Chemical Physics Letters: X*, 2019, **3**, 100030.
88 R. García-Meseguer and B. K. Carpenter, *European Journal of Organic Chemistry*, 2019, **2019**, 254–266.
89 S. Naik and S. D. Ross, *Commun. Nonlinear Sci.*, 2017, **47**, 48–70.
90 M. Topaler and N. Makri, *The Journal of Chemical Physics*, 1994, **101**, 7500–7519.
91 J. E. Straub, M. Borkovec and B. J. Berne, *The Journal of Chemical Physics*, 1986, **84**, 1788–1794.
92 B. Bagchi and D. W. Oxtoby, *The Journal of Chemical Physics*, 1983, **78**, 2735–2741.
93 W. S. Koon, M. W. Lo, J. E. Marsden and S. D. Ross, *Dynamical systems, the three-body problem and space mission design*, Marsden books, 2011, p. 327.
94 T. S. Parker and L. O. Chua, *Practical Numerical Algorithms for Chaotic Systems*, Springer-Verlag New York, Inc., New York, NY, USA, 1989.
95 K. R. Meyer, G. R. Hall and D. Offin, *Introduction to Hamiltonian Dynamical Systems and the N-Body Problem*, Springer, 2009.
96 J. E. Marsden and S. D. Ross, *Bulletin of the American Mathematical Society*, 2006, **43**, 43–73.
97 S. Wiggins, L. Wiesenfeld, C. Jaffé and T. Uzer, *Physical Review Letters*, 2001, **86**, 5478.
98 J. A. J. Madrid and A. M. Mancho, *Chaos*, 2009, **19**, 013111.
99 A. Junginger, G. T. Craven, T. Bartsch, F. Revuelta, F. Borondo, R. Benito and R. Hernandez, *Physical Chemistry Chemical Physics*, 2016, **18**, 30270–30281.

100 A. Junginger and R. Hernandez, *The Journal of Physical Chemistry B*, 2016, **120**, 1720–1725.

101 A. Junginger, L. Duvenbeck, M. Feldmaier, J. Main, G. Wunner and R. Hernandez, *The Journal of chemical physics*, 2017, **147**, 064101.

102 A. Junginger, J. Main, G. Wunner and R. Hernandez, *Phys. Rev. A*, 2017, **95**, 032130.

103 C. Lopesino, F. Balibrea, S. Wiggins and A. M. Mancho, *Communications in Nonlinear Science and Numerical Simulation*, 2015, **27**, 40–51.

104 G. T. Craven, A. Junginger and R. Hernandez, *Physical Review E*, 2017, **96**, 022222.

105 G. T. Craven and R. Hernandez, *Physical Chemistry Chemical Physics*, 2016, **18**, 4008–4018.

106 G. T. Craven and R. Hernandez, *Physical review letters*, 2015, **115**, 148301.

107 R. Bardakcioglu, A. Junginger, M. Feldmaier, J. Main and R. Hernandez, *Phys. Rev. E*, 2018, **98**, 032204.

108 M. Feldmaier, P. Schraft, R. Bardakcioglu, J. Reiff, M. Lober, M. Tschöpe, A. Junginger, J. Main, T. Bartsch and R. Hernandez, *The Journal of Physical Chemistry B*, 2019, **123**, 2070–2086.

109 J. D. Meiss, *Chaos: An Interdisciplinary Journal of Nonlinear Science*, 1997, **7**, 139–147.

Appendices

A Details of the De Leon-Berne Hamiltonian

The potential energy function for the system dynamics can be broken down into three terms that models a conformational isomerization in the $y-$coordinate by a double well potential, $V_{\mathrm{DW}}(y)$, a dissociation in the $x-$coordinate by a Morse potential, $V_{\mathrm{M}}(y)$, and a coupling term, $V_{\mathrm{DWM}}(x,y)$ to write

$$\begin{aligned} V_{\mathrm{DB}}(x,y) =& V_{\mathrm{DW}}(y)+V_{\mathrm{M}}(x)+V_{\mathrm{DWM}}(x,y) \\ V_{\mathrm{DW}}(y) =& \frac{\mathscr{V}^{\ddagger}}{y_w^4}y^2(y^2-2y_w^2)+\varepsilon_s \\ V_{\mathrm{M}}(x) =& D_x\left[1-\exp(-\lambda x)\right]^2 \\ V_{\mathrm{DWM}}(x,y) =& \frac{\mathscr{V}^{\ddagger}}{y_w^4}y^2(y^2-2y_w^2)\left[\exp(-\zeta\lambda x)-1\right] \end{aligned} \tag{14}$$

where the parameters are

$\mathscr{V}^{\ddagger}$: potential energy difference between the isomerization barrier and the bottom of the well for $\zeta = 0$.

fix $y_w = \pm 1/\sqrt{2}$: location of the isomerization wells (symmetric about the $y = 0$ axis).

fix $\varepsilon_s = 1.0$: potential energy of the barrier.

fix $D_x = 10.0$: dissociation energy of the Morse potential.

vary λ : range of the Morse potential.

vary ζ : coupling strength between the Morse potential and the double well potential.

Symmetries of the equations of motion — We note the symmetries in the system (4), by substituting $(-y,-p_y)$ for (y,p_y) which implies reflection about the $x-$axis ($y = 0$ line) and expressed as

$$s_y : (x,y,p_x,p_y,t) \to (x,-y,p_x,-p_y,t) \tag{15}$$

Furthermore, the energy conservative Hamiltonian system (4) has time-reversal symmetry given by

$$s_t : (x,y,p_x,p_y,t) \to (x,y,-p_x,-p_y,-t) \tag{16}$$

So, if $(x(t),y(t),p_x(t),p_y(t))$ is a solution to (4), then combining the two symmetries s_y and s_t, we can assert $(x(-t),y(-t),-p_x(-t),-p_y(-t))$ is another solution. These symmetries can be used to decrease the number of computations, and to find special solutions. For example, any solution of (4) will evolve on the energy surface given by (2). For fixed energy, $\mathscr{H}(x,y,p_x,p_y) = E$, there will be zero velocity curves corresponding to $V_{\mathrm{DB}}(x,y) = E$ contours as shown in Fig. 1. Any trajectory which touches the zero velocity curve (boundary in phase space where kinetic energy is zero) at time t_0 must retrace its path in configuration space (i.e. $q = (x,y)$ space),

$$q(-t+t_0) = q(t+t_0) \qquad \mathring{q}(-t+t_0) = -\mathring{q}(t+t_0) \tag{17}$$

This fact is useful in finding the unstable periodic orbit located in the bottleneck of the Hamiltonian[4,26,27].

Hill's region and zero velocity curve— The projection of the energy surface onto the configuration space, the (x,y) plane, is the region of energetically possible motion for a given total energy, E. Let $M(E)$ denote this projection* and defined as

$$M(E) = \left\{(x,y) \in \mathbb{R}^2 \,|\, V_{\mathrm{DB}}(x,y) \leqslant E\right\}, \tag{18}$$

where $V_{\mathrm{DB}}(x,y)$ is the potential energy (14). The projection of the energy surface onto the configuration space, the (x,y) plane, is known historically in mechanics as the *Hill's region* and the boundary of $M(E)$ is known as the *zero velocity curve*. This projection denotes the bounds on the motion for a fixed energy and can be used to visualize configurations allowed by energetically accessible motion in high-dimensional phase space[76]. Furthermore, the zero velocity curve is the locus of the points in the (x,y) plane where the kinetic energy is zero, that is

$$\mathscr{H}(x,y,p_x,p_y) = E = \frac{1}{2}\left(\frac{p_x^2}{m_x}+\frac{p_y^2}{m_y}\right)+V_{\mathrm{DB}}(x,y) \tag{19}$$

$$\left(\frac{p_x^2}{m_x}+\frac{p_y^2}{m_y}\right) = 2(E-V_{\mathrm{DB}}(x,y)) = 0 \tag{20}$$

Thus, the motion is only possible on the side of this curve where the kinetic energy is positive and the other side is *energetically*

* It is to be noted that our convention is to use script letters for a region in the energy surface (including the energy surface itself, $\mathscr{M}$) and italicized capital letters for that region's projection onto the configuration space (for example, M)

forbidden and shown as grey region in the configuration space in the Fig. 3.

B Computational method for the unstable periodic orbit and its cylindrical invariant manifolds

We consider the dynamics of the conservative system by determining the phase space "skeleton" that governs transition between potential well (or, equivalently escape from a well). In the simplest case of only two degrees of freedom, the phase space is of four dimensional and the boundary between potential wells is defined using unstable periodic orbit that lie in the bottleneck connecting the wells. The set of all states leading to escape from a potential well can be understood as residing within an invariant manifold of geometry $\mathbb{R}^1 \times \mathbb{S}^1$, that is a cylinder or tube. The interior of this tube defines the set of all states which will transition to the adjacent well.

B.1 Linearization at the index-1 saddle

It is to be noted that the linearization of the behavior of trajectories near the saddle-center equilibrium points appears in the leading order expression of the transition fraction. We are interested in trajectories which have an energy just above that of the critical value. The region of possible motion for $E > E_c$ contains a neck around each saddle equilibrium point. The geometry of trajectories close to the neck region is studied by considering the linearized equations of motion near the equilibrium point.

Let $\mathbf{x}_{\rm eq}$ denote the equilibrium point connecting the top and bottom wells. Furthermore, for a fixed energy E, we consider a neighborhood of $\mathbf{x}_{\rm eq}$ on the energy surface, whose configuration space projections are the bottleneck regions. We refer to this neighborhood as the *equilibrium region* and denote it by $\mathscr{R}$ on the energy surface. We perform a coordinate transformation with $\mathbf{x}_{\rm eq} = (x_{\rm eq}, y_{\rm eq}, 0, 0)$ as the new origin, and keep the first order terms, we obtain

$$\dot{\mathbf{x}} = \mathbb{J}(\mathbf{x}_{\rm eq})\mathbf{x} \qquad \text{where,} \qquad \mathbf{x} = [x, y, p_x, p_y]^T \tag{21}$$

where $\mathbb{J}(\mathbf{x}_{\rm e,1})$ is the Jacobian of the Hamiltonian vector field (4) evaluated at the equilibrium point. The Jacobian involves derivatives of Eqns. (14) and the kinetic energy does not depend on the position coordinates, we can write compactly

$$\mathbb{J}(\mathbf{x}) = D\mathbf{f}(\mathbf{x}) = \begin{pmatrix} 0 & 0 & 1/m_x & 0 \\ 0 & 0 & 0 & 1/m_y \\ -\frac{\partial^2 \mathscr{H}}{\partial x^2} & -\frac{\partial^2 \mathscr{H}}{\partial y \partial x} & 0 & 0 \\ -\frac{\partial^2 \mathscr{H}}{\partial x \partial y} & -\frac{\partial^2 \mathscr{H}}{\partial y^2} & 0 & 0 \end{pmatrix} \tag{22}$$

$$= \begin{pmatrix} 0 & 0 & 1/m_x & 0 \\ 0 & 0 & 0 & 1/m_y \\ -\frac{\partial^2 V_{DB}}{\partial x^2} & -\frac{\partial^2 V_{DB}}{\partial y \partial x} & 0 & 0 \\ -\frac{\partial^2 V_{DB}}{\partial x \partial y} & -\frac{\partial^2 V_{DB}}{\partial y^2} & 0 & 0 \end{pmatrix} \tag{23}$$

Thus, the linearized vector field at the equilibrium point becomes

$$\dot{\mathbf{x}} = \mathbb{J}(\mathbf{x}_{\rm eq})\mathbf{x} = D\mathbf{f}(\mathbf{x}_{\rm eq}) = \begin{pmatrix} 0 & 0 & 1/m_x & 0 \\ 0 & 0 & 0 & 1/m_y \\ -2D_x\lambda^2 & 0 & 0 & 0 \\ 0 & \frac{4\mathscr{V}^{\ddagger}}{y_w^2} & 0 & 0 \end{pmatrix} \mathbf{x} \tag{24}$$

where $\mathbf{f}$ denotes the Hamiltonian vector field, that is the right hand side of the Hamilton's equations. It can be checked that the eigenvalues of the Jacobian to be of the form $\lambda, -\lambda, i\omega, -i\omega$ with $\lambda > 0$, $\omega > 0$ and given by

$$\lambda = \sqrt{\frac{4\mathscr{V}^{\ddagger}}{m_y y_w^2}}, \quad \omega = \sqrt{\frac{2D_x\lambda^2}{m_x}}, \tag{25}$$

with corresponding eigenvectors given by

$$\begin{aligned} u_{\pm\lambda} &= \left[0, \quad 1, \quad 0, \quad \pm\sqrt{\frac{4\mathscr{V}^{\ddagger} m_y}{y_w^2}}\right] \\ u_{i\pm\omega} &= \left[1, \quad 0, \quad \pm i\sqrt{2D_x\lambda^2 m_x}, \quad 0\right] \end{aligned} \tag{26}$$

Thus, the general (real) solution of (21) has the form

$$\mathbf{x}(t) = (x(t), y(t), p_x(t), p_y(t)) \tag{27}$$

$$= \alpha_1 e^{\lambda t} u_\lambda + \alpha_2 e^{-\lambda t} u_{-\lambda} + 2\mathrm{Re}(\beta e^{i\omega t} u_{i\omega}) \tag{28}$$

where, α_1, α_2 are real and $\beta = \beta_1 + i\beta_2$ is complex.

B.2 Numerical method for computing reactive islands

Step 1: Select appropriate energy above the critical value — For computing the unstable periodic orbits and its invariant manifolds that are phase space conduits for transition between the two isomers, we have to specify a total energy, E, that is above the energy of the index-1 saddle (this is referred to as critical energy or reference energy or isomerization energy, E_c, in the chemical reaction dynamics literature) and so the excess energy $\Delta E = E - E_c > 0$. This excess energy can be arbitrarily large as long as the unstable periodic orbit does not bifurcate.

Step 2: Compute the unstable periodic orbit associated with the rank-1 saddle — We consider a procedure which computes unstable periodic orbits associated with rank-1 saddle in a straightforward fashion. This procedure begins with small "seed" initial conditions obtained from the linearized equations of motion near $\mathbf{x}_{\rm eq}$, and uses differential correction and numerical continuation to generate the desired periodic orbit corresponding to the chosen energy $E = \varepsilon_s + \Delta E$ [93]. The result is a periodic orbit of the desired energy E of some period T, which will be close to $2\pi/\omega$ where $\pm\omega$ is the imaginary pair of eigenvalues of the linearization around the saddle point.

Guess for initial condition of a periodic orbit — The general solution of linearized equations of motion (Eqn. (28)) at the equilibrium point $\mathbf{x}_{\rm eq}$ can be used to initialize a guess for an iterative correction procedure called *differential correction*. The linearization yields an eigenvalue problem $Av = \gamma v$, where A is the Jacobian

matrix evaluated at the equilibrium point, γ is the eigenvalue, and $v = [k_1, k_2, k_3, k_4]^T$ is the corresponding eigenvector. We initialize the guess for the periodic orbit for a small amplitude, $A_x << 1$. Let $\beta = -A_x/2$ and using the eigenvector spanning the center subspace, we can guess the initial condition to be

$$\bar{\mathbf{x}}(0) = \bar{\mathbf{x}}_{0,\mathrm{g}} = (x_{0,g}, y_{0,g}, p_{x_{0,g}}, p_{y_{0,g}})^T \tag{29}$$

$$= (x_{\mathrm{eq}}, y_{\mathrm{eq}}, 0, 0)^T + 2Re(\beta u_{i\omega}) = (x_{\mathrm{eq}} - A_x, y_{\mathrm{eq}}, 0, 0)^T \tag{30}$$

Differential correction of the initial condition — In this *iterative correction* procedure, we introduce small change in the guess for the initial condition such that coordinates at the final and initial time of the periodic orbit

$$\left\| \bar{\mathbf{x}}_{\mathrm{po}}(T) - \bar{\mathbf{x}}_{\mathrm{po}}(0) \right\| < \varepsilon \tag{31}$$

for some tolerance $\varepsilon << 1$. In this approach, we hold $x-$coordinate constant, while applying correction to the initial guess of the $y-$coordinate, use p_x-coordinate for terminating event-based integration, and p_y-coordinate to test convergence of the periodic orbit. It is to be noted that a specific combination of the phase space coordinates is only suitable for potential, and in general will require some permutation of the coordinates to achieve a stable algorithm.

Let us denote the flow map of a differential equation $\mathring{\mathbf{x}} = \mathbf{f}(\mathbf{x})$ with an initial condition $\mathbf{x}(t_0) = \mathbf{x}_0$ by $\phi(t; \mathbf{x}_0)$. Thus, the displacement of the final state under a perturbation δt becomes

$$\delta\bar{\mathbf{x}}(t + \delta t) = \phi(t + \delta t; \bar{\mathbf{x}}_0 + \delta\bar{\mathbf{x}}_0) - \phi(t; \bar{\mathbf{x}}_0) \tag{32}$$

with respect to the reference orbit $\bar{\mathbf{x}}(t)$. Thus, measuring the displacement at $t_1 + \delta t_1$ and expanding into Taylor series gives

$$\delta\bar{\mathbf{x}}(t_1 + \delta t_1) = \frac{\partial\phi(t_1; \bar{\mathbf{x}}_0)}{\partial \mathbf{x}_0}\delta\bar{\mathbf{x}}_0 + \frac{\partial\phi(t_1; \bar{\mathbf{x}}_0)}{\partial t_1}\delta t_1 + h.o.t \tag{33}$$

where the first term on the right hand side is the state transition matrix, $\Phi(t_1, t_0)$, when $\delta t_1 = 0$. Thus, it can be obtained as numerical solution to the variational equations as discussed in [94]. Let us suppose we want to reach the desired point $\mathbf{x}_{\mathrm{d}}$, we have

$$\bar{\mathbf{x}}(t_1) = \phi(t_1; \bar{\mathbf{x}}_0) = \bar{\mathbf{x}}_1 = \mathbf{x}_d - \delta\bar{\mathbf{x}}_1 \tag{34}$$

which has an error $\delta\bar{\mathbf{x}}_1$ and needs correction. This correction to the first order can be obtained from the state transition matrix at t_1 and an iterative procedure of this small correction based on first order yields convergence in few steps. For the equilibrium point under consideration, we initialize the guess as

$$\bar{\mathbf{x}}(0) = (x_{0,g}, y_{0,g}, p_{x_{0,g}}, p_{y_{0,g}})^T = (-A_x, 0, 0, 0)^T \tag{35}$$

and using numerical integrator we continue until next $p_x = 0$ event crossing with a high specified tolerance (typically 10^{-14}). So, we obtain $\bar{\mathbf{x}}(t_1)$ which for the guess periodic orbit denotes the half-period point, $t_1 = T_{0,g}/2$ and compute the state transition matrix $\Phi(t_1, 0)$. This can be used to correct the initial value of $y_{0,g}$ to approximate the periodic orbit while keeping $x_{0,g}$ constant. Thus, correction to the first order is given by

$$\delta p_{x_1} = \Phi_{32}\delta y_0 + \mathring{p}_{x_1}\delta t_1 + h.o.t \tag{36}$$

$$\delta p_{y_1} = \Phi_{42}\delta y_0 + \mathring{p}_{y_1}\delta t_1 + h.o.t \tag{37}$$

where Φ_{ij} is the $(i,j)^{th}$ entry of $\Phi(t_1, 0)$ and the acceleration terms come from the equations of motion evaluated at the crossing $t = t_1$ when $p_{x_1} = \delta p_{x_1} = 0$. Thus, we obtain the first order correction δy_0 as

$$\delta y_0 \approx \left(\Phi_{42} - \Phi_{32}\frac{\mathring{p}_{y_1}}{\mathring{p}_{x_1}}\right)^{-1}\delta p_{y_1} \tag{38}$$

$$y_0 \to y_0 - \delta y_0 \tag{39}$$

which is iterated until $|p_{y_1}| = |\delta p_{y_1}| < \varepsilon$ for some tolerance ε, since we want the final periodic orbit to be of the form

$$\bar{\mathbf{x}}_{t_1} = (x_1, y_1, 0, 0)^T \tag{40}$$

This procedure yields an accurate initial condition for a periodic orbit of small amplitude $A_x << 1$, since our initial guess is based on the linear approximation near the equilibrium point. It is also to be noted that differential correction assumes the guess periodic orbit has a small error (for example in this system, of the order of 10^{-2}) and can be corrected using first order form of the correction terms. If, however, larger steps in correction are applied this can lead to unstable convergence as the half-orbit overshoots between successive steps. Even though there are other algorithms for detecting unstable periodic orbits, differential correction is easy to implement and shows reliable convergence for generating a dense family of periodic orbits (UPOs) associated with the rank-1 saddle at arbitrary high excess energy (as long as UPOs don't bifurcate). These unstable perioidic orbit at high excess energy are required for constructing codimension-1 invariant manifolds.

Numerical continuation to unstable periodic orbit at an arbitrary energy — The above procedure yields an accurate initial condition for a unstable periodic orbit from a single initial guess. If our initial guess came from the linear approximation near the equilibrium point, from Eqn. (28), it has been observed in the numerics that we can only use the differential correction procedure for small amplitude ($\sim 10^{-4}$) periodic orbit around $\mathbf{x}_e$. This small amplitude corresponds to small excess energy, typically $\sim 10^{-2}$, and to find an unstable periodic orbit of arbitrarily large amplitude, we resort to the procedure of *numerical continuation* to generate a family which reaches the appropriate energy E. Numerical continuation uses the two small amplitude periodic orbits obtained from the differential correction procedure and proceeds as follows.

Suppose we find two small nearby periodic orbit initial conditions, $\bar{\mathbf{x}}_0^{(1)}$ and $\bar{\mathbf{x}}_0^{(2)}$, correct to within the tolerance d, using the differential correction procedure described above. We can then generate a family of periodic orbits with successively increasing amplitudes associated with the rank-1 saddle $\bar{\mathbf{x}}_{\mathrm{e}}$ in the following way. Let

$$\Delta = \bar{\mathbf{x}}_0^{(2)} - \bar{\mathbf{x}}_0^{(1)} = [\Delta x_0, \Delta y_0, 0, 0]^T \tag{41}$$

A linear extrapolation to an initial guess of slightly larger amplitude, $\bar{\mathbf{x}}_0^{(3)}$ is given by

$$\bar{\mathbf{x}}_{0,g}^{(3)} = \bar{\mathbf{x}}_0^{(2)} + \Delta \tag{42}$$

$$= \left[(\mathbf{x}_0^{(2)} + \Delta x_0), (y_0^{(2)} + \Delta y_0), 0, 0\right]^T \tag{43}$$

$$= \left[x_0^{(3)}, y_0^{(3)}, 0, 0\right]^T \tag{44}$$

Now, we can use differential correction to refine the guess initial condition $\bar{\mathbf{x}}_{0,g}^{(3)}$ until a specified tolerance is satisfied. Then, we repeat using $\bar{\mathbf{x}}_0^{(3)}$ and $\bar{\mathbf{x}}_0^{(2)}$ to obtain the next $\bar{\mathbf{x}}_0^{(4)}$, so on and so forth until we have a family of solutions. We can keep track of the energy of each periodic orbit and when we have two solutions, $\bar{\mathbf{x}}_0^{(\mathrm{k})}$ and $\bar{\mathbf{x}}_0^{(\mathrm{k+1})}$, whose energy bisects the desired target energy, E_{target}, we halt the numerical continuation of the family. Next, we resort to combining bisection and differential correction to the last two periodic orbits until we converge to the unstable periodic orbit at E_{target} to within a specified tolerance. Thus, the result is a periodic orbit at E_{target} and of some period T_{po} with an initial condition $\bar{\mathbf{x}}_0$.

Step 3: Globalization of the invariant manifolds — First, we find the local approximation to the unstable and stable manifolds of the periodic orbit from the eigenvectors of the monodromy matrix. Next, the local linear approximation of the unstable (or stable) manifold in the form of a state vector is integrated in the nonlinear equations of motion to produce the approximation of the unstable (or stable) manifolds. This procedure is known as *globalization of the manifolds* and we proceed as follows

First, the state transition matrix $\Phi(t)$ along the periodic orbit with initial condition $\bar{\mathbf{x}}_0$ can be obtained numerically by integrating the variational equations along with the equations of motion from $t = 0$ to $t = T$. This is known as the monodromy matrix $M = \Phi(T)$ and the eigenvalues can be computed numerically. The theory for Hamiltonian systems (see Ref.[95] for details) tells us that the four eigenvalues of M are of the form

$$\lambda_1 > 1, \qquad \lambda_2 = \frac{1}{\lambda_1}, \qquad \lambda_3 = \lambda_4 = 1 \tag{45}$$

The eigenvector associated with eigenvalue λ_1 is in the unstable direction, the eigenvector associated with eigenvalue λ_2 is in the stable direction. Let $e^s(\bar{\mathbf{x}}_0)$ denote the normalized (to 1) stable eigenvector, and $e^u(\bar{\mathbf{x}}_0)$ denote the normalized unstable eigenvector. We can compute the stable manifold and unstable manifold at $\bar{\mathbf{x}}_0$ by initializing along the eigenvectors

$$X^{s/u}(\bar{\mathbf{x}}_0) = \bar{\mathbf{x}}_0 + \varepsilon e^{s/u}(\bar{\mathbf{x}}_0). \tag{46}$$

Here the small displacement from $\bar{\mathbf{x}}_0$ is denoted by ε and its magnitude should be small enough to be within the validity of the linear estimate, yet not so small that the time of flight becomes too large due to asymptotic nature of the stable and unstable manifolds. Ref.[93] suggests typical values of $\varepsilon > 0$ corresponding to nondimensional position displacements of magnitude around 10^{-6}. By numerically integrating the unstable vector forwards in time, using both ε and $-\varepsilon$, for the two branches emanating from the NHIM, respectively, we generate trajectories shadowing the two branches, W_+^u and W_-^u, of the unstable manifold of the NHIM. Similarly, by integrating the stable vector backwards in time, using both ε and $-\varepsilon$, for forward and backward branch respectively, we generate trajectories shadowing the stable manifold, $W_{+,-}^s$. For the manifold at $X(t)$, one can simply use the state transition matrix to transport the eigenvectors from X_0 to $X(t)$:

$$X^{s/u}(X(t)) = \Phi(t,0)X^{s/u}(\bar{\mathbf{x}}_0) \tag{47}$$

It is to be noted that since the state transition matrix does not preserve the norm and so the resulting vector must be normalized. The globalized invariant manifolds associated with rank-1 saddles are known as Conley-McGehee tubes and these spherical cylinders form the impenetrable barriers and phase space conduits for transition between potential wells[96,97].

C Lagrangian descriptor

In the original form[60,98], the Lagrangian descriptor (LD) is the arc length of a trajectory with initial conditions $\mathbf{x}_0$ at time t_0 and integrated for a fixed time, τ, in forward or backward direction. Recently, an alternate formulation has been developed[74] for continuous time dynamical systems to prove results on detecting invariant phase space structures using singular features in the LD contour map.

In the general setting of a non-autonomous vector field

$$\frac{d\mathbf{x}}{dt} = \mathbf{v}(\mathbf{x},t), \quad \mathbf{x} \in \mathbb{R}^n\,,\ t \in \mathbb{R} \tag{48}$$

where $\mathbf{v}(\mathbf{x},t) \in C^r$ $(r \geq 1)$ in $\mathbf{x}$ and continuous in time. The definition of the LD depends on the initial condition $\mathbf{x}_0 = \mathbf{x}(t_0)$, on the initial time t_0 (trivial for autonomous systems), the integration time τ, and the type of norm used in the form below:

$$M_p(\mathbf{x}_0,t_0,\tau) = \int_{t_0-\tau}^{t_0+\tau} \sum_{i=1}^{n} |\dot{x}_i(t;\mathbf{x}_0)|^p\, dt \tag{49}$$

where $p \in (0,1]$ and $\tau \in \mathbb{R}^+$ are freely chosen parameters, and the overdot represents the derivative with respect to time. It is to be noted here that there are three formulations of the function M_p in the literature: the arc length of a trajectory in phase space[60,98], the arc length of a trajectory projected on the configuration space[99–102], and the sum of the p-norm of the vector field components[74,103]. This latter formulation which does not resemble the arc length of a trajectory, and yet has been shown to identify the NHIM and its stable and unstable manifolds with the singular features and minima (or maxima) in the contour map for benchmark systems in recent work by the authors[75,76]. Thus, it follows from the numerical verifications and theoretical proof that

$$\mathscr{W}^s(\mathbf{x}_0,t_0) = \operatorname{argext} \mathscr{L}^{(f)}(\mathbf{x}_0,t_0,\tau) \tag{50}$$

$$\mathscr{W}^u(\mathbf{x}_0,t_0) = \operatorname{argext} \mathscr{L}^{(b)}(\mathbf{x}_0,t_0,\tau) \tag{51}$$

where the stable and unstable manifolds ($\mathscr{W}^s(\mathbf{x}_0,t_0)$ and $\mathscr{W}^u(\mathbf{x}_0,t_0)$) denote the invariant manifolds at intial time t_0 and

argext $(\cdot)$ denotes the argument that minimizes (or maximizes) the function $\mathscr{L}^{(\cdot)}(\mathbf{x}_0,t_0,\tau)$ in forward and backward time, respectively. In addition, the coordinates on the NHIM, $\mathscr{M}(\mathbf{x}_0,t_0)$, at time t_0 is given by the intersection $\mathscr{W}^s(\mathbf{x}_0,t_0)$ and $\mathscr{W}^u(\mathbf{x}_0,t_0)$ of the stable and unstable manifolds, and thus given by

$$\begin{aligned}\mathscr{M}(\mathbf{x}_0,t_0) &= \text{argext}\left(\mathscr{L}^{(f)}(\mathbf{x}_0,t_0,\tau)+\mathscr{L}^{(b)}(\mathbf{x}_0,t_0,\tau)\right)\\ &= \text{argext}\,\mathscr{L}(\mathbf{x}_0,t_0,\tau)\end{aligned} \tag{52}$$

In applying the LD method to nonlinear systems, one observes multiple singularities and extremal values that can lead to ambiguities with isolating the extremas corresponding to the NHIM and the ones due to the invariant manifolds[76,101]. This computational issue can be addressed by using another formulation and has been used to locate transition state trajectories for driven two degrees of freedom and three degrees of freedom chemical reaction models[104–106]. It has been observed in numerical experiments that computing fixed integration time Lagrangian descriptor (LD) as given by Eqn. (49) leads to two potential issues:

1. Bounded trajectories will show global recrossings of the barrier as predicted by the Poincaré recurrrence theorem for a bounded energy surface. The recrossings will show multiple minima and singularities in the LD contour map which obscures locating the actual NHIM[76,101].

2. The trajectories that escape the open potential well will leave with ever increasing acceleration, if the potential energy surface opens out to infinity. These trajectories will have large LD values (compared to the bounded trajectories) and will render the contour map flat which again obscures locating the NHIM.

To circumvent these issues, a heuristic that has been adopted[76,101,107,108] is to calculate LD values only until a trajectory remains inside the *preselected* barrier region. As a result, the initial conditions on an invariant manifold will show as singularities and maxima in the LD contour map because of being integrated for the full integration time interval, τ, which others which leave the region will have smaller LD values.

Thus, the formulation of Eqn. (49) can be modified as

$$M_p(\mathbf{x}_0,t_0,\tau^{\pm}) = \int_{t_0-\tau^-}^{t_0+\tau^+}\sum_{i=1}^{n}|\dot{x}_i(t;\mathbf{x}_0)|^p\,dt \tag{53}$$

where the integration time interval, τ, depends on a trajectory and is given by

$$\tau^{\pm}(\mathbf{x}_0) = \min\left(\tau, t|_{|\mathbf{x}(t)|>q_s}\right) \tag{54}$$

where q_s defines the *preselected* barrier region in the configuration space around the saddle in the bottleneck. We note here that the only initial condition that gets integrated for the full time interval τ units in forward and backward time is the one on the NHIM. In addition, the coordinates on the NHIM, $\mathscr{M}(\mathbf{x}_0,t_0)$, at time t_0 is given by

$$\begin{aligned}\mathscr{M}(\mathbf{x}_0,t_0) &= \text{argmax}\left(\mathscr{L}^{(f)}(\mathbf{x}_0,t_0,\tau)+\mathscr{L}^{(b)}(\mathbf{x}_0,t_0,\tau)\right)\\ &= \text{argmax}\,\mathscr{L}(\mathbf{x}_0,t_0,\tau)\end{aligned} \tag{55}$$

The variable integration time Lagrangian descriptor as given by Eqn. (53) to locate invariant manifolds is familiar to the dynamical systems community and is related to computing average exit times to locate invariant sets in the phase space of symplectic maps[109].

D Discretization of the Spectral Density: Derivation of the Parameters of the Bath

The coupling of the bath of harmonic oscillators to the configuration space coordinates is described by a spectral density:

$$J_x(\omega) = \frac{\pi}{2}\sum_{i=1}^{N_B}\frac{c_{x,i}^2}{\omega_i}\delta(\omega-\omega_i), \tag{56}$$

$$J_y(\omega) = \frac{\pi}{2}\sum_{i=1}^{N_B}\frac{c_{y,i}^2}{\omega_i}\delta(\omega-\omega_i), \tag{57}$$

and these result from the discretization of a continuous Ohmic (linear) form with an exponential cutoff:

$$\bar{J}_x(\omega) = \eta_x\omega e^{-\frac{\omega}{\omega_c}}, \tag{58}$$

$$\bar{J}_y(\omega) = \eta_y\omega e^{-\frac{\omega}{\omega_c}}, \tag{59}$$

the discretization that gives us the coupling constants $c_{x,j}$, $c_{y,j}$, and the frequencies ω_j, and are given by

$$\omega_j = -\omega_c\log\left(\frac{j-\frac{1}{2}}{N_B}\right), \quad j=1,\ldots,N_B. \tag{60}$$

and

$$c_{x,j} = \sqrt{\frac{2\eta_x\omega_c}{\pi N_B}}\,\omega_j, \tag{61}$$

$$c_{y,j} = \sqrt{\frac{2\eta_y\omega_c}{\pi N_B}}\,\omega_j, \quad j=1,\ldots,N_B. \tag{62}$$

In this appendix we describe a scheme for discretizing the continuous spectral density which was given in Craig and Manolopoulos[59]. In the following we will drop the subscripts x and y on the various quantities for the sake of a simpler notation since we will follow the same discretization procedure for each spectral density. The subscripts can then be added back afterwards. Re-establishing the notation, the discrete spectral density function is given by:

$$J(\omega) = \frac{\pi}{2}\sum_{i=1}^{N_B}\frac{c_i^2}{\omega_i}\delta(\omega-\omega_i), \tag{63}$$

and the continuous spectral density is given by:

$$\bar{J}(\omega) = \eta\,\omega e^{-\frac{\omega}{\omega_c}}. \tag{64}$$

Discretization is obtained by carrying out the following steps.

1. Require

$$\int_0^\infty J(\omega)F(\omega)d\omega \approx \int_0^\infty \bar{J}(\omega)F(\omega)d\omega, \qquad (65)$$

for any integrable function $F(\omega)$

2. Substitute (63) into the left-hand side of (65) to obtain:

$$\frac{\pi}{2}\sum_{i=1}^{N_B}\frac{c_i^2}{\omega_i}F(\omega_i). \qquad (66)$$

3. Approximate the right-hand side of (65) by an appropriate quadrature. This is the step that we will now carry out in detail.

The quadrature recommended in[59] is the midpoint rule, after changing variables in the integral to $x = e^{-\frac{\omega}{\omega_c}}$. The reason that they give for choosing this quadrature is that it gives a uniform distribution of grid points in the unit interval $0 < x_i < 1$ and therefore a logarithmic distribution of bath frequencies $\omega_i = -\omega_c \log x_i$. They claim that such a distribution of bath frequencies is appropriate on physical grounds for an exponentially decaying density of bath states.

The change of variables gives:

$$x = e^{-\frac{\omega}{\omega_c}} \Rightarrow \log x = -\frac{\omega}{\omega_c} \Rightarrow \omega = -\omega_c \log x, \qquad (67)$$

$$dx = -\frac{1}{\omega_c}e^{-\frac{\omega}{\omega_c}}d\omega = -\frac{1}{\omega_c}x d\omega. \qquad (68)$$

Then (64) becomes

$$\bar{J}(\omega) = -\eta x \omega_c \log x, \qquad (69)$$

and using this expression, and the change of variables given in (67) and (68), the right-hand side of (65) becomes:

$$-\int_0^1 \eta\omega_c^2(\log x)F(\omega(x))dx. \qquad (70)$$

We discretize this integral using the midpoint rule. We partition the unit interval into N_B intervals of length $\frac{1}{N_B}$ and evaluate the integrand at the midpoint, x_i, of each sub-interval:

$$x_i = \frac{i-\frac{1}{2}}{N_B}, i = 1,\ldots,N_B, \qquad (71)$$

and obtain:

$$-\int_0^1 \eta\omega_c^2(\log x)F(\omega(x))dx \approx -\sum_{i=1}^{N_B}\eta\omega_c^2\log x_i F(\omega(x_i))\frac{i}{N_B}. \qquad (72)$$

Equating each term in the sum (66) to each term in the sum (72) gives:

$$\frac{\pi}{2}\frac{c_i^2}{\omega_i} = -\frac{1}{N_B}\eta\omega_c^2\log x_i = \frac{1}{N_B}\eta\omega_c\omega_i,$$

which gives:

$$c_i = \sqrt{\frac{2\eta\omega_c}{\pi N_B}}\,\omega_i, \quad i = 1,\ldots,N_B. \qquad (73)$$

and from (67) and (71) we see that:

$$\omega_i = -\omega_c \log\left(\frac{i-\frac{1}{2}}{N_B}\right), \quad i = 1,\ldots,N_B. \qquad (74)$$

E Linear stability analysis of the system-bath dynamics

As noted in the article, the location of the equilibrium points in the system-bath model are dependent on the frequencies and coupling strength of the bath modes. Hence, we would like to analyze the stability of these equilibrium points. The Jacobian of the system-bath Hamiltonian vector field (8) is

$$\mathbb{J} = \left(\begin{array}{c|c} \mathbf{0} & \mathbf{M} \\ \hline \frac{\partial^2 V_{\mathrm{SB}}}{\partial x_i x_j} & \mathbf{0} \end{array}\right),$$

$$\text{where } i,j = 1,2,\ldots,N_S(N_B+1) \qquad (75)$$

where each block matrix is of size $N_S(N_B+1)\times N_S(N_B+1)$. The matrix $\mathbf{M}$ is given by:

$$\mathbf{M} = \begin{pmatrix} \frac{1}{m_s} & 0 & 0 & 0 & 0 & \cdots & \cdots & \cdots & \cdots & 0 \\ 0 & \frac{1}{m_s} & 0 & 0 & 0 & \cdots & \cdots & \cdots & \cdots & 0 \\ 0 & 0 & \frac{1}{m_1} & 0 & 0 & \cdots & \cdots & \cdots & \cdots & 0 \\ 0 & 0 & 0 & \frac{1}{m_2} & 0 & \cdots & \cdots & \cdots & \cdots & 0 \\ 0 & 0 & 0 & 0 & \ddots & \cdots & \cdots & \cdots & \cdots & 0 \\ 0 & 0 & 0 & 0 & 0 & \cdots & \frac{1}{m_1} & 0 & \cdots & 0 \\ 0 & 0 & 0 & 0 & 0 & \cdots & 0 & \frac{1}{m_2} & \cdots & 0 \\ 0 & 0 & 0 & 0 & 0 & \cdots & \cdots & \cdots & \ddots & 0 \end{pmatrix}$$

$$\frac{\partial^2 V_{\mathrm{SB}}}{\partial} = \begin{pmatrix} -\frac{\partial^2 V_{\mathrm{DB}}}{\partial x^2} - \sum_j (\frac{c_{x,j}}{\omega_j})^2 & -\frac{\partial^2 V_{\mathrm{DB}}}{\partial y \partial x} & c_{x,1} & c_{x,2} & \cdots & c_{x,N_B} & 0 & 0 & \cdots & 0 \\ -\frac{\partial^2 V_{\mathrm{DB}}}{\partial y \partial x} & -\frac{\partial^2 V_{\mathrm{DB}}}{\partial y^2} - \sum_j (\frac{c_{y,j}}{\omega_j})^2 & 0 & 0 & \cdots & 0 & c_{y,1} & c_{y,2} & \cdots & c_{y,N_B} \\ c_{x,1} & 0 & -\omega_1^2 & 0 & \cdots & 0 & 0 & 0 & \cdots & 0 \\ c_{x,2} & 0 & 0 & -\omega_2^2 & \cdots & 0 & 0 & 0 & \cdots & 0 \\ \vdots & 0 & 0 & 0 & \ddots & 0 & 0 & 0 & \cdots & 0 \\ c_{x,N_B} & 0 & 0 & 0 & \cdots & -\omega_{N_B}^2 & 0 & 0 & \cdots & 0 \\ 0 & c_{y,1} & 0 & 0 & \cdots & 0 & -\omega_1^2 & 0 & \cdots & 0 \\ 0 & & & & & & & & & \end{pmatrix}$$

where $\mathbf{M}$ is a diagonal matrix with mass of system and bath degrees of freedom along the main diagonal and $\frac{\partial^2 V_{\mathrm{SB}}}{\partial x_i x_j}$ is the Hessian of the potential energy function for the system-bath model.

The Jacobian evaluated at the equilibrium points $\bar{x}$ is given by

$$\mathbb{J}(\bar{q}) = \left(\begin{array}{c|c} \mathbf{0} & \mathbf{M} \\ \hline \frac{\partial^2 V_{\mathrm{SB}}}{\partial x_i x_j}(\bar{q}) & \mathbf{0} \end{array}\right),$$

$$\text{where } i,j = 1,2,\ldots,N_S(N_B+1) \tag{76}$$

The eigenvalues are given by the solutions of the characteristic equation:

$$\det\left(\mathbb{J}(\bar{\mathrm{q}}) - \lambda\mathbb{I}\right) = 0 \tag{77}$$

where $\mathbb{J}(\bar{q})$ and $\mathbb{I}$ are $2N_S(N_B+1)\times 2N_S(N_B+1)$ matrices.

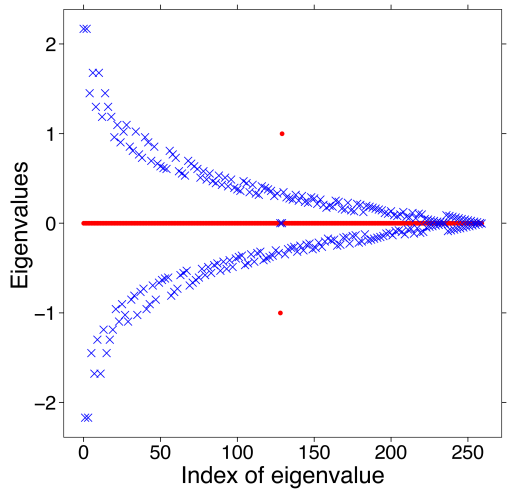

Fig. 10 Eigenvalues of the equilibrium point $\bar{q}_s$ of the system-bath model (8) where the real part is shown as red dots and imaginary part is shown as blue cross. The pair (positive and negative) of purely real eigenvalues verify the equilibrium point is an index-1 saddle. For this case, bath parameters used are $m_i = 1.0, \eta_x = \eta_y = 0.1, \omega_c = \sqrt{5}, N_B = 64$ and the y-axis is normalized by the square of the cut-off frequency, ω_c.

For $N_B = 64$, the eigenvalues are plotted in the Fig. 10 where all the real components are zero except for the one pair that corresponds to the $\pm\lambda$ eigenvalues and the imaginary components (frequencies) of the eigenvalues shown as blue crosses show the exponential decay expected from the spectral density (58) and (59).

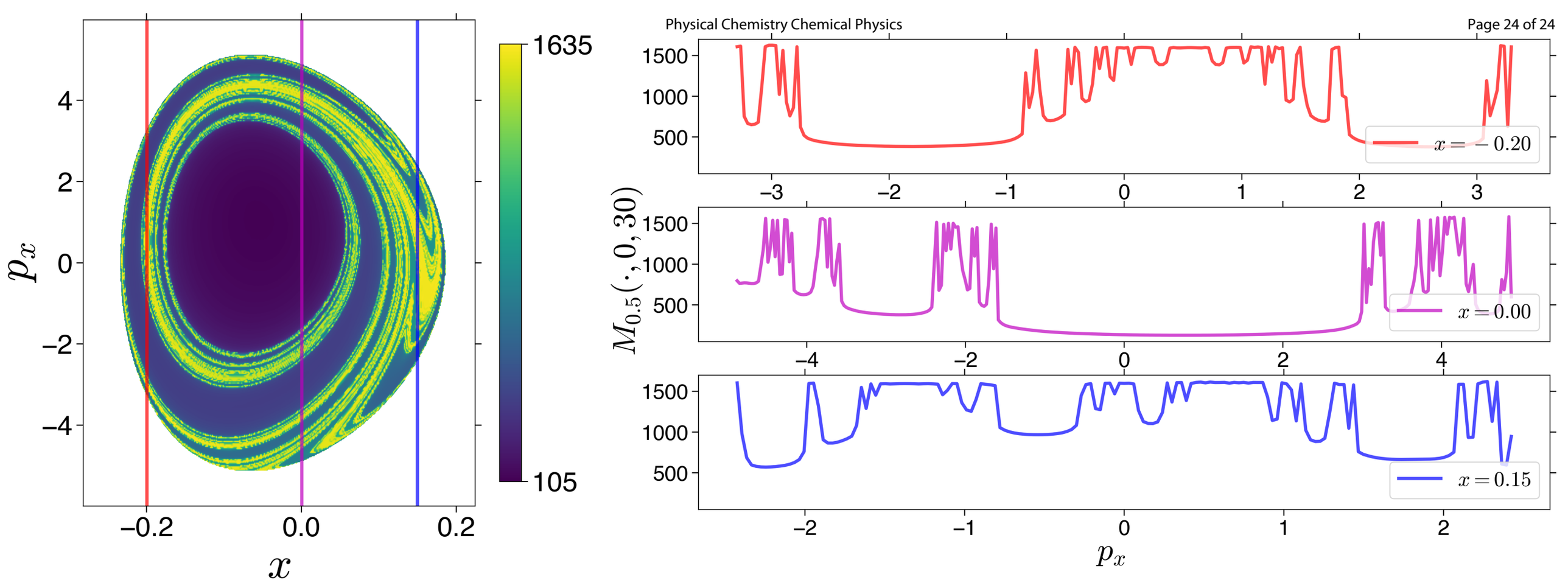

Reactive islands in a system-bath model of isomerization detected by the singular features in the Lagrangian descriptor contour map